frontiers | Frontiers in Earth Science

TYPE Original Research
PUBLISHED 29 July 2025
DOI 10.3389/feart.2025.1576938

OPEN ACCESS

EDITED BY
Simona Ferrando,
University of Turin, Italy

REVIEWED BY
Javier García Serrano,
Complutense University of Madrid, Spain
Chiara Groppo,
University of Turin, Italy

*CORRESPONDENCE
Brian O'Driscoll,
brian.odriscoll@uottawa.ca

RECEIVED 14 February 2025
ACCEPTED 03 July 2025
PUBLISHED 29 July 2025

CITATION
O'Driscoll B and Henry H (2025) Transient corundum stability in high-temperature metamorphic mineral assemblages: insights from the British Paleogene Igneous Province. *Front. Earth Sci.* 13:1576938.
doi: 10.3389/feart.2025.1576938

Transient corundum stability in high-temperature metamorphic mineral assemblages: insights from the British Paleogene Igneous Province

Brian O'Driscoll[1]* and Hadrien Henry[2,3]

[1]Department of Earth and Environmental Sciences, University of Ottawa, Ottawa, ON, Canada, [2]Géosciences Environnement Toulouse, Université de Toulouse III Paul Sabatier, Toulouse, France, [3]ARC Centre of Excellence for Core to Crust Fluid System (CCFS) and GEMOC, Department of Earth and Planetary Sciences, Macquarie University, Sydney, NSW, Australia

Samples containing corundum-anorthite-hercynite are examined to better understand the crystallisation history of this assemblage. These minerals are commonly observed together in the products of high temperature (pyro-)metamorphism of aluminous protoliths. However, it is not clear if they are an equilibrium paragenesis and, if not, whether there is a consistent relative order of crystallisation of the minerals. The physical state of the medium crystallising these phases is also not well understood, with suggested possibilities including crystallisation in the solid state, in refractory Al-rich melts and in systems undergoing melt-rock reaction. Here we investigate the microstructure of the corundum-anorthite-hercynite assemblage in a well-known example from the Loch Scridain Sill Complex (Isle of Mull; ~60 Ma British Paleogene Igneous Province, NW Scotland), where the rocks of interest comprise crustal xenoliths in a basaltic sill. Another less well-known occurrence from Ardnamurchan, where magmatism is also associated with the British Paleogene Igneous Province, is investigated too. Our combined mineral chemical and electron backscatter diffraction dataset reveal that corundum is a transient phase in both lithologies. The Ardnamurchan rocks comprise discrete oxide (hercynite)- and plagioclase-rich portions, and exhibit macro- and microstructural features interpreted here as forming in a crystal mush, possibly following crystallisation from two immiscible (relatively Fe- and Si-rich) liquids. There is a close crystallographic relationship between corundum and ilmenite in these rocks, with the latter replacing the former in the interstitial spaces between hercynite crystals in the oxide-rich portions of the sample. Corundum in the Mull xenolithic samples exhibits a distinctive texture where hercynite pseudomorphs dendritic and skeletal crystals of the former without apparent changes in the volume or shape of the crystals. This reaction is attributed to infiltration of melt into the xenolith, with consequent conversion of corundum to hercynite. However, the corundum crystal habits and the coarse-grained oikocrystic plagioclase in which they occur are suggestive of crystallisation from an original refractory Al-rich melt phase. Comparisons of the textures observed here with corundum-anorthite-spinel from other settings, including in Archean anorthosites and in corundum-magnetite rocks (emery),

suggest that replacement of corundum by spinel may be a ubiquitous process in these rocks.

KEYWORDS

corundum, hercynite, British Paleogene Igneous Province, pyrometamorphism, melting

Introduction

The corundum-anorthite-spinel (*sensu lato*) assemblage is a relatively common product of the high temperature contact metamorphism of aluminous protoliths, as well as a number of other geological settings (*e.g.*, metamorphosed Precambrian anorthosites, reaction coronae on corundum xenocrysts; Karmakar et al., 2017; Karmakar et al., 2020; van Hinsberg et al., 2021; Schuster et al., 2023). In the case where a high temperature metamorphic origin is clear, it is generally considered that the paragenesis forms in relatively low silica, refractory (Al-rich) residues, following the mobilisation of granitic melts and consequent relative loss of Ca, Na and K (Grapes, 2011). This tenet, that corundum saturation is due to residual enrichment rather than Al-mobilisation, is supported by workers studying corundum petrogenesis in other settings as well (*e.g.*, metasomatic formation; van Hinsberg et al., 2021). Aluminous xenoliths entrained in mafic magmas have received particular attention because they shed important light on processes associated with crustal anatexis, including granitic melt production and the crustal contamination of mafic magmas (*e.g.*, Preston et al., 1999; Markl, 2005; Mariga et al., 2006a; Mariga et al., 2006b). Indeed, it has been proposed that corundum-anorthite-spinel rims around buchite (where buchite is a term for a vitreous rock produced by contact metamorphism)-cored xenoliths represent an analogue for Proterozoic anorthosites, potentially formed when mafic magmas interacted with Al-rich rocks at the base of the crust (Dempster et al., 1999). In any case, although it is not always straightforward to make the connections between processes operating on sub-metre-to-metre sized xenoliths and crustal scale processes or even between xenoliths and >km sized intrusions and their country rocks (Markl, 2005), studies of the corundum-anorthite-spinel assemblage in aluminous xenoliths have yielded valuable insights into disequilibrium mineral growth (Markl, 2005; Mariga et al., 2006a) and stepwise melting of Al-rich rocks (Preston et al., 1999).

Complexity and lack of uniformity in the reaction-driven processes during formation of corundum-anorthite-spinel parageneses is implied from the details provided in a number of studies. For example, Preston et al. (1999) interpreted the occurrence of this assemblage in ~cm-thick rims around aluminous xenoliths from the Paleogene Isle of Mull igneous centre (Scotland) as the product of crystallisation from a H_2O-free, Al-rich melt followed by crystal scale mixing of this melt with invading basalt from the xenolith host rocks. The xenolith rims studied by Preston et al. (1999) occur around relatively small (maximum 80 mm diameter) mullite buchite xenoliths, and the authors invoked an intricate mixing process operating in isolated pockets interstitial to plagioclase to produce corundum and spinel in these rocks. Markl (2005) studied aluminous xenoliths hosted in marginal rocks of the Paleogene Skaergaard layered intrusion (Greenland) and though developed a similar model to that of Preston et al. (2009), elucidated a more complex series of disequilibrium melting + crystallisation processes in the formation of corundum. An early stage is considered to have been associated with corundum crystallisation in a residuum, together with plagioclase, spinel, cordierite and sillimanite/mullite, following granitic melt formation and extraction. Entrainment of these residual fragments led to formation of an immiscible Al-rich melt and a second stage of corundum crystallisation (together with rutile, mullite, plagioclase, spinel, tridymite and cordierite). Late-stage interaction of these xenoliths with their basaltic host led to ingress of Fe and Mg and a number of reactions, including breakdown of corundum to form spinel. Finally, Mariga et al. (2006a); Mariga et al., (2006b) described the formation of the corundum-anorthite-spinel assemblage in xenolithic quartzofeldspathic gneiss leucosomes incorporated into the basaltic magmas that formed the Mesoproterozoic Voisey's Bay intrusion (Canada). They argued for crystallisation of corundum in an Al-rich restitic material that either underwent 2-stage melt removal or disequilibrium melting. Mariga et al. (2006a) documented spectacular pseudomorphs of skeletal hercynite after corundum in their xenoliths, that they attributed to late-stage reaction of corundum with the host basaltic melt.

In addition to apparently all involving subtle but important variations in process, the studies described above serve to highlight that the corundum-anorthite-spinel paragenesis is not necessarily considered to be an equilibrium assemblage. There is also some uncertainty as to whether these minerals crystallise from Al-rich melts or in solid restite, an important question to resolve from the point of view of the types of reactions taking place. In this study we report the results of a combined microstructural-mineral chemical investigation of two classic pyrometamorphic mineral assemblage localities, Glebe Hill in Ardnamurchan and the Rudh' a' Chromain sill on the Isle of Mull, both in NW Scotland and associated with igneous centres of the British Paleogene Igneous Province. Electron backscatter diffraction (EBSD) provides quantitative information on crystallographic orientations and can thus provide insight into the nucleation and growth of minerals in rocks (cf. Prior et al., 1999). In this contribution, we present new EBSD data together with mineral chemistry and petrographic observations on rocks from the Mull and Ardnamurchan localities, with the aim of addressing some of the uncertainty in the crystallisation history of the corundum-anorthite-spinel paragenesis. In particular, recognising that no two such occurrences are identical, an important goal is to shed some light on the timing of crystallisation of the individual phases and the physical state of the protolith during corundum-anorthite-spinel crystallisation.

Geological setting and sample provenance

British Paleogene Igneous Province (BPIP)

The British Paleogene Igneous Province (BPIP) is part of the larger Northeast Atlantic Igneous province and formed at ~60 Ma during opening of the NE Atlantic Ocean and the onset of melting associated with the mantle plume currently situated under Iceland (Bell and Williamson, 2002; Emeleus and Bell, 2005). In addition to flood basalt lava fields and a NW-SE trending regional dyke swarm, the BPIP comprises a suite of roughly north-south trending igneous centres that mainly occur along the northwest coast of Scotland. The igneous centres postdate the flood basalts, predate the dyke swarm and are believed to represent the exposed shallow level (1–2 km) intrusions that manifested at the surface as volcanoes. The centres comprise a broad range of intrusion geometries and magma compositions and have been intensely studied from the complementary perspectives of magmatic differentiation and sub-volcanic system architecture for more than 160 years (Geikie, 1861; Geikie, 1897; Harker, 1904; Bailey et al., 1924; Richey and Thomas, 1930; Bell and Williamson, 2002; Emeleus and Bell, 2005). The BPIP magmatism spanned a number of terrane boundaries so the igneous centres also intrude a spatially and temporally diverse array of crustal rocks, depending on their location. On Mull and Ardnamurchan, the two igneous centres of interest here (Figure 1), the country rocks comprise a condensed sequence of Mesozoic sedimentary rocks that unconformably overlie Neoproterozoic metasedimentary rocks of the Moine Supergroup, which in turn likely overlie (were thrust over) Archean rocks of the Lewisian Complex (Emeleus and Bell, 2005). A major terrane bounding structure, the Great Glen Fault, runs through the southeast of Mull meaning that rocks of the Neoproterozoic Dalradian Supergroup, which lie to the south of that structure, are also in close proximity to the Mull igneous centre.

Glebe Hill, Ardnamurchan

The Glebe Hill corundum locality was documented and described in some detail by Richey and Thomas (1930), but has received comparatively little attention since then (*e.g.*, Wells, 1951; Gribble, 1976; Day, 1989). The rocks occur in a restricted (10 × 20 m) zone on the southern (outer) margin of the so-called Hypersthene Gabbro, a component intrusion of the Ardnamurchan igneous centre and one of the purported Centres of magmatic activity there (Figure 1a; Richey and Thomas, 1930; Day, 1989; Emeleus and Bell, 2005). The corundum-bearing lithologies are poorly exposed, but exhibit a distinctive appearance in which cm-scale spinel-rich clots and schlieren occur in a plagioclase-rich matrix (Figure 2a). The spinel-rich areas are chaotically distributed throughout the exposure, in some instances defining an irregular layering in the rock, and in other instances defining no fabric at all. The high modal concentration (>50 mod.%) of spinel (identified as hercynite and magnetite by Richey and Thomas, 1930) was taken to imply a high Fe concentration in the protolith which, together with their aluminous nature led Richey and Thomas (1930) toward the possibility that high-temperature metamorphism of a laterite soil, produced by weathering of basalt lava, was the process responsible for the development of the plagioclase-corundum-spinel assemblage. Thomas (in Richey and Thomas, 1930) interpreted the broader distribution of hornfels as representing irregularly-shaped metre-scale masses (*i.e.*, separate xenoliths), whereas Richey (in the same volume) interpreted these as screens. What is clear is that at Glebe Hill, the plagioclase-corundum-spinel-bearing material occurs as rafts within rocks previously described as granulitic-textured (contact metamorphosed, recrystallised) basalts (Richey and Thomas, 1930), and not within the younger main mass of the Hypersthene Gabbro, although the contact is closeby (within metres; Day, 1989).

The sample studied here (Ard-B-2) comes from an exposure such as that shown in Figure 2a. The main criterion in selecting this sample for further study was the clear evidence for two components in the rock, *i.e.*, the spinel-rich and plagioclase-rich portions, as well as the presence of corundum, all at the scale of an individual thin section.

Rudh' a' Chromain, Mull

The Rudh' a' Chromain sill is part of the Loch Scridain Sill Complex (LSSC; Preston et al., 1998), associated with the Isle of Mull igneous centre of the BPIP (Figure 1b), and has been the subject of numerous petrological investigations for nearly a century (*e.g.*, Thomas, 1922; Bailey et al., 1924; Buist, 1959; Buist, 1961; Preston and Bell, 1997; Preston et al., 1999; Preston, 2001). The Rudh' a' Chromain sill is composite, comprising a rhyolitic core that grades without obvious discontinuity into basaltic margins at its top and bottom, and is intruded into sandstone at its lower contact and an earlier monzonite intrusion at its upper contact (Figure 1c; Thomas, 1922; Preston, 2001). Xenoliths of various character occur throughout the sill, including cognate (gabbroic) and metasedimentary materials, but are mainly concentrated in its basaltic outer portions. The aluminous xenoliths of interest here are concentrated in the inner part of the upper basaltic zone (Figures 2b,c; Thomas, 1922), and were subdivided by Buist (1961) into two main types: mullite-buchites and plagioclase-corundum-spinel assemblages. Thomas (1922) and Buist (1961) both showed that the plagioclase-corundum-spinel assemblage occurs and thus formed as the modified outer portions of the mullite-buchite xenoliths, even though our observations indicate that fragments composed exclusively of plagioclase-corundum-spinel also occur, but this is presumably as a result of disaggregation of 'whole' xenoliths. This observation aligns with the general classification of Preston et al. (1999), who highlighted the importance of plagioclase-rich rims on mullite-buchite xenoliths throughout the LSSC. Preston et al. (1999) also discussed the potential protoliths for the LSSC xenoliths and concluded that Al-rich pelitic schists of the Moine Supergroup are the most likely candidates. Other possibilities, such as Paleogene laterites and Jurassic mudstones, were dismissed by the latter authors for reasons of there being no evidence of the consequent high Fe content that should be observed and the fact that aluminous xenoliths are found in sills that intrude the Moine Supergroup, below the structural level that Jurassic sedimentary rocks crop out at on Mull.

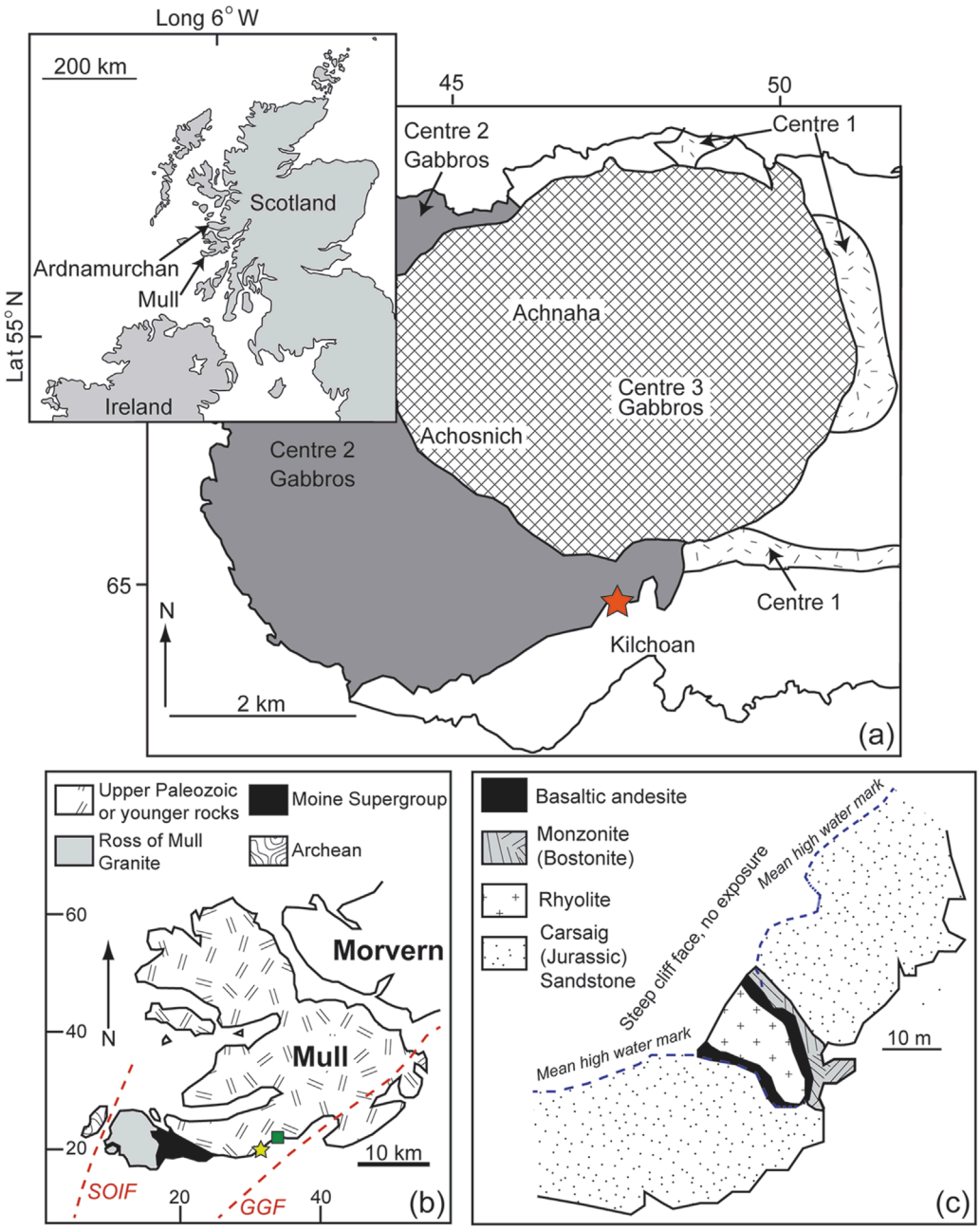

FIGURE 1
Location maps for the studied samples. **(a)** Simplified map of the geology of western Ardnamurchan peninsula, with inset showing the regional setting of both Ardnamurchan and Mull in NW Scotland. The red star marks the Glebe Hill locality, close to the boundary between the putative Centres 1 and 2 rocks. The map is adapted from one in O'Driscoll (2007). **(b)** Simplified geological map of the Isle of Mull, showing the major lithological subdivisions and structural features. The green square and yellow star mark the position of Carsaig and the Rudh' a' Chromain sill, respectively. **(c)** Detailed sketch map of the Rudh' a' Chromain sill, adapted from Preston (2001). SOIF, Sound of Iona Fault; GGF, Great Glen Fault.

Sample Mu-B-4 comes from a portion of the Rudh' a' Chromain sill that contains numerous, relatively small (<3 cm diameter) fragments of the outer plagioclase-rich rims to the mullite-buchite xenoliths. Since the corundum-related assemblage is the primary focus of the present study, a suitable xenolith was selected from this sample for detailed work and the buchite portions of the xenoliths were not considered further.

Petrography

Thorough overviews of the petrographic variation observed amongst the aluminous xenoliths in the Rudh' a' Chromain sill are provided by Thomas (1922) and Buist (1961), and a detailed description of the Glebe Hill assemblage is given in Richey and Thomas (1930). Here we focus solely on the petrography of the two samples studied, Ard-B-2 and Mu-B-4, each of which is

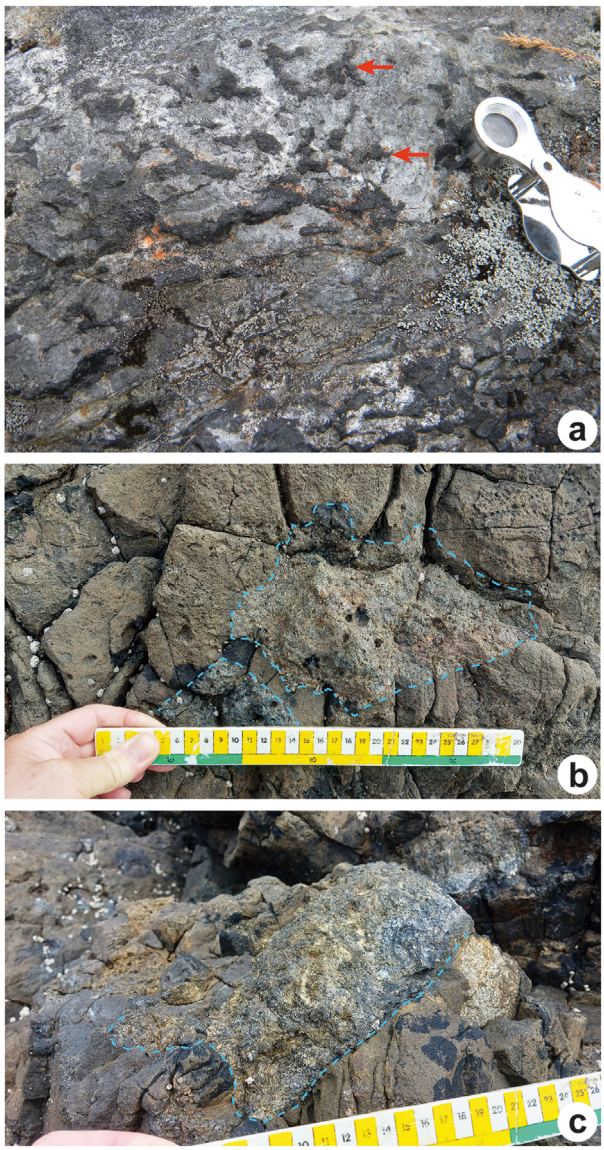

FIGURE 2
Field photographs of the Glebe Hill and Rudh' a' Chromain localities. **(a)** Outcrop of the Glebe Hill exposure showing spinel-rich clots and lensoid masses (two examples highlighted with red arrows) in an anorthositic groundmass. The handlens shown for scale is ~6 cm long. **(b,c)** Examples of corundum-anorthite-spinel xenoliths in the Rudh' a' Chromain sill. The irregular margins of the xenoliths are highlighted with blue dashed lines and the ruler is marked at the centimeter scale.

represented by one thin section that was the target for the analytical work performed here. However, from our general observations on outcrops and other thin sections from both localities, the mineralogy and microstructure in Ard-B-2 and Mu-B-4 are characteristic and the two samples are representative of each of their respective lithologies.

Glebe Hill–sample Ard-B-2

The subdivision of the rock into mm-to-cm-thick spinel-rich and plagioclase-rich portions, apparent from field observations, dominates the rock texture at the thin section scale (Figure 3a). The evidence for secondary alteration is limited to fine-grained, or partly amorphous, several hundred micron diameter, irregularly-shaped patches in the rock, described below, that do not constitute more than 5 modal % of the sample. We concur with Day (1989) that no magnetite exists in this rock and that, in addition to plagioclase-corundum-hercynite, ilmenite makes up a significant proportion (~10 mod.%) of the rock. The plagioclase-rich portions of the rock are mainly characterised by relatively fine-grained stubby plagioclase crystals that share clean, straight grain boundaries with no evidence of a shape-preferred orientation of grains (Figure 3b). Plagioclase twin boundaries are well-defined, cross-cut the entire grains and are straight, and individual crystals sporadically exhibit oscillatory zoning (see Figure 3b). Fine grained (10s of μm), rounded hercynite crystals are abundant as inclusions in some areas of the plagioclase-rich zones, with a slight preference to be concentrated toward crystal cores (Figure 3b). Locally, plagioclase crystals are coarser-grained (up to 1 mm long); this occurs in cm-sized pockets of hercynite-rich material within the plagioclase-rich areas or at the contacts with pockets of fine-grained or amorphous material that also occur sporadically throughout the sample.

Most of the spinel in the rock is hercynite (~40 mod.% of the rock). It mainly forms relatively coarse-grained (grain sizes up to 0.5 mm) equant and polygonal crystals that comprise massive aggregates in irregularly shaped clots and schlieren (Figures 3a,c). Hercynite grain sizes tend to decrease by an order of magnitude at the margins of the schlieren. No plagioclase is observed in the hercynite-rich parts of the sample. The margins of the hercynite-rich zones are also characterised by the occurrence of the amorphous material referred to above. Ilmenite is evenly distributed throughout the plagioclase-rich portions of the rock, and occurs as coarser-grained aggregates intergrown with hercynite in the spinel-rich parts. In the latter, ilmenite is anhedral and exhibits concave crystal boundaries against hercynite. Hercynite-hercynite-ilmenite apparent (2D) dihedral angles in these portions of the samples are low (typically <45°). Corundum comprises a small proportion (<5 mod.%) of the studied sample, and is mainly present within the spinel-rich portions of the sample (Figure 3c). It can occur as clusters of euhedral crystals exhibiting an impingement texture, but more commonly is distributed as isolated single or a few crystals throughout the hercynite-dominated portions of the sample (Figures 3c,d). Some larger euhedral corundum grains contain inclusions of hercynite that are restricted to the outer parts of the crystal (Figure 3d). Where not present in the oxide-rich parts of the sample, corundum occurs as fine-grained material closely associated with ilmenite in the interstitial spaces between plagioclase crystals. The corundum is often closely spatially associated with the occurrences of the fine-grained or amorphous material in the sample (Figure 3c). The amorphous patches are brownish-coloured in plane-polarised light, appear to be glassy in part, can also exhibit a cloudy/turbid appearance in which the outlines of plagioclase crystals are observed (Figure 3e), and contain patches of fine-grained micaceous aggregates that appear to be sericite. Richey and Thomas (1930) reported fine-grained mullite needles at the edges of plagioclase crystals and pseudomorphs after cordierite in the amorphous patches. We observed the mullite needles in some parts of our sample, but did not observe

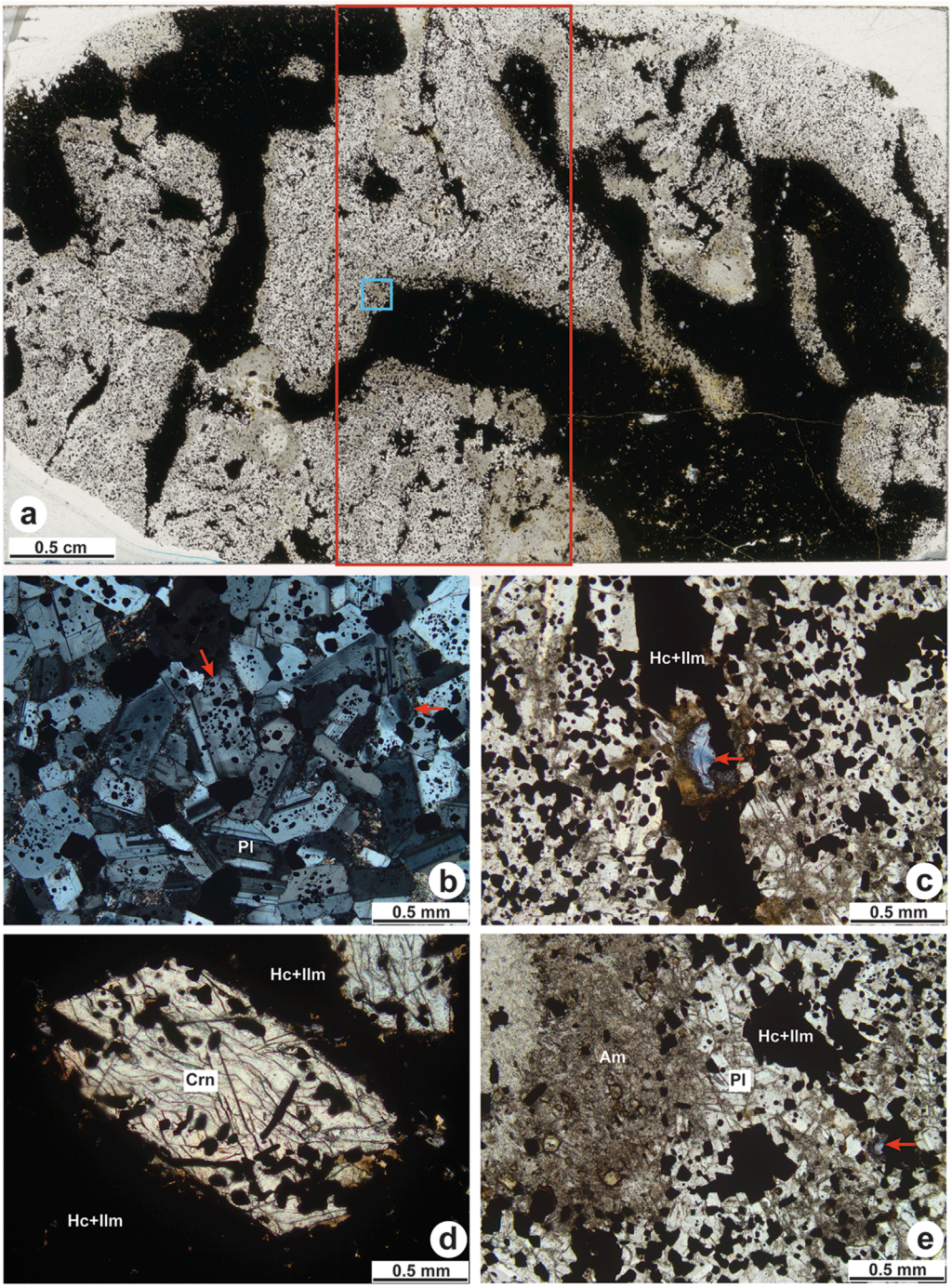

FIGURE 3
Photomicrographs of Glebe Hill sample Ard-B-2. **(a)** Scan of the thin section studied, with the area examined in detail demarcated by the red rectangle. The blue box shows the location of the backscattered electron image shown in Figure 5a. **(b)** Cross polarised light image of plagioclase-rich portion in Ard-B-2, showing the distribution of hercynite within plagioclase crystals. Note that hercynite seems to be preferentially concentrated in some plagioclase cores. Note also that some plagioclase crystals appear optically zoned (two examples highlighted by red arrows). **(c)** A thin hercynite (plus ilmenite) seam runs vertically through the middle of this photomicrograph, in an otherwise plagioclase-hercynite rich groundmass. Note the corundum crystal (blue, highlighted with red arrow) hosted within the seam, in a pocket of brownish coloured amorphous material. Photomicrograph taken in plane-polarised light. **(d)** Plane-polarised light view of a euhedral corundum crystal hosted within a hercynite-rich portion of the sample. Note the presence of irregularly-shaped hercynite as inclusions in a mantle around the edges of the crystal, but their comparative sparsity in the crystal centre. The corundum in the top right of the image exhibits a faint blueish colour. **(e)** Plane-polarised light image of the boundary between a plagioclase-rich portion of Ard-B-2, containing clots of hercynite, with an area of fine-grained and amorphous material (labelled Am) in which sparse hercynite, some a greenish colour, occurs. Note the corundum in the hercynite clot furthest to the right (arrowed). Mineral abbreviations as follows: Crn, corundum; Hc, hercynite; Ilm, ilmenite; Pl, plagioclase.

cordierite (or any textures we could confidently relate to its prior existence).

Rudh' a' Chromain—sample Mu-B-4

The Rudh' a' Chromain sample studied in detail here is a small xenolith about 2.5 cm and 0.5–1 cm long and wide, respectively (Figure 4a). The mineralogy predominantly comprises the plagioclase-corundum-hercynite assemblage of interest. The xenolith outer margins are ragged and irregular; there are local truncations of individual elongate corundum and hercynite crystals and spaces between crystals close to the margins contain groundmass material that may be connected to the exterior in three dimensions. Relatively large sulfide (0.5–1 cm) and calcite (0.1–0.5 cm) crystals are sporadically distributed around and attached to the xenolith margins. The groundmass comprises mainly evenly-distributed diopside, plagioclase and Fe-oxide in a medium-grained intergranular, isotropic texture. Secondary alteration is limited to local saussuritisation of plagioclase in the xenolith along sparse veinlets and grain boundaries, as well as in fine-grained patches of the groundmass host.

The xenolith can be subdivided into two portions, on the basis of texture and mineralogy, that comprise about 50% of the sample area each. However, based on our petrographic observations of at least 10 other xenoliths, this subdivision appears to reflect a general distinction and is not restricted to just our xenolith. The first portion contains skeletal corundum crystals embedded in large (up to 1 cm diameter) plagioclase oikocrysts (*e.g.*, Figure 4b). Small portions (<10%) of some corundum crystals are perfectly pseudomorphed by hercynite. In the other portion of the xenolith, skeletal hercynite crystals of very similar form and dimensions to the corundum occur. The converse relationship is observed, with small portions (<20%) of these crystals comprising corundum, without any change in the shape or surface area of the hercynite. The hercynite is also embedded in plagioclase, but there are a greater number of smaller oikocrysts in this part of the xenolith. In some instances, plagioclase inclusions within skeletal hercynite crystals have twin interfaces oriented differently to those plagioclase crystals immediately outside the hercynite. Well-developed multiple twin sets in plagioclase in this and the other portion of the xenolith are tapered and no optical zoning is observed. Two types of fine-grained material occur in interstitial pockets in the xenolith: (1) containing rock that is texturally and mineralogically identical to the host groundmass, and more common in the second portion of the xenolith; (2) areas of brown-coloured devitrified glassy material that contains dense clusters of mullite needles, and more common in the corundum-rich portion of the xenolith (Figure 4d). Ilmenite is present as a very low abundance phase in the second portion of the xenolith, where it forms part of the hercynite-corundum skeletal crystals, apparently also in a pseudomorphing relationship (Figure 4e). No preferred orientation of either hercynite or corundum is apparent anywhere in the xenolith.

Analytical techniques

Mineral chemistry by scanning electron microscope and electron microprobe

Backscattered electron imaging of regions of interest, *i.e.*, the amorphous patches in Ard-B-2, was carried out using a Tescan Vega 4 electron microscope at Géosciences Environnement Toulouse. Images were acquired using a 15 KeV acceleration voltage and a working distance of ~15 mm. Electron microprobe analyses were carried out using a Cameca SX-Five at the Centre de Microcaractérisation Raimond Castaing (Toulouse, France). The accelerating voltage used was 15 kV, the beam current 20 nA, the electron beam diameter 1 µm and the counting time 10 s on peak and 5 s on backgrounds on both sides of the peak. The following synthetic and natural minerals standards were used: periclase (Mg), corundum (Al), pyrophanite (Mn, Ti), hematite (Fe), chromium oxide (Cr), pure nickel (Ni), sphalerite (Zn), pure vanadium (V). The detection limits are 0.03 wt% for TiO_2, Al_2O_3, Cr_2O_3, MgO, 0.06 wt% for V_2O_3 and NiO, and 0.07% for FeO (referred to as Fe_{Total}), MnO, ZnO. The internal precision (% relative standard deviation) is better than 2% for Cr, Mg, Al, Fe and better than 6% for TiO_2.

Electron backscatter diffraction analysis and mapping

Thin sections were prepared for electron backscatter diffraction (EBSD) analysis by polishing for 2 hours using a solution of colloidal silica in a Buhler Vibromet polisher before a ~5 nm thick coat of carbon was applied to prevent charging during analysis. Crystallographic orientations were acquired by indexing diffraction patterns with a CMOS symmetry S2 detector (Oxford Instrument) attached to a FEG JEOL JSM 7100F scanning electron microscope in the Centre de Microcaractérisation Raimond Castaing in Toulouse (France). Samples were tilted at a 68°–70° angle and a 20 kV accelerating voltage was used. Working distance ranged from 25 mm for large area mapping to 15 mm for the higher resolution maps. Step size and magnification varied depending on the map and the sample. Two high resolution maps of regions of interest in Ard-B-2 were made at 0.75 and 2 µm step sizes with a magnification of 400 and 200, respectively. Larger maps, representing a third of the thin section area for Ard-B-2 and the whole xenolith for Mu-B-4, were made at step sizes of 10 and 15 µm, respectively, with a magnification of 75.

EBSD data were preprocessed using the Aztec Crystal software; this included removing wild spikes and extrapolating pixels with 8, 7 and 6 identical neighbours. The cleaned data were then processed in MATLAB using the MTex toolbox (Bachmann et al., 2011; Bachmann et al., 2010; following the protocol described in Henry, 2018). Analyses with a mean angular deviation greater than 1.3° were discarded. Grains were determined using 10° as the cut-off angle. All Euler orientation maps, reflecting the mean orientation of the grains, were produced to elucidate microstructural characteristics of the samples. For each sample, the mean orientation of each

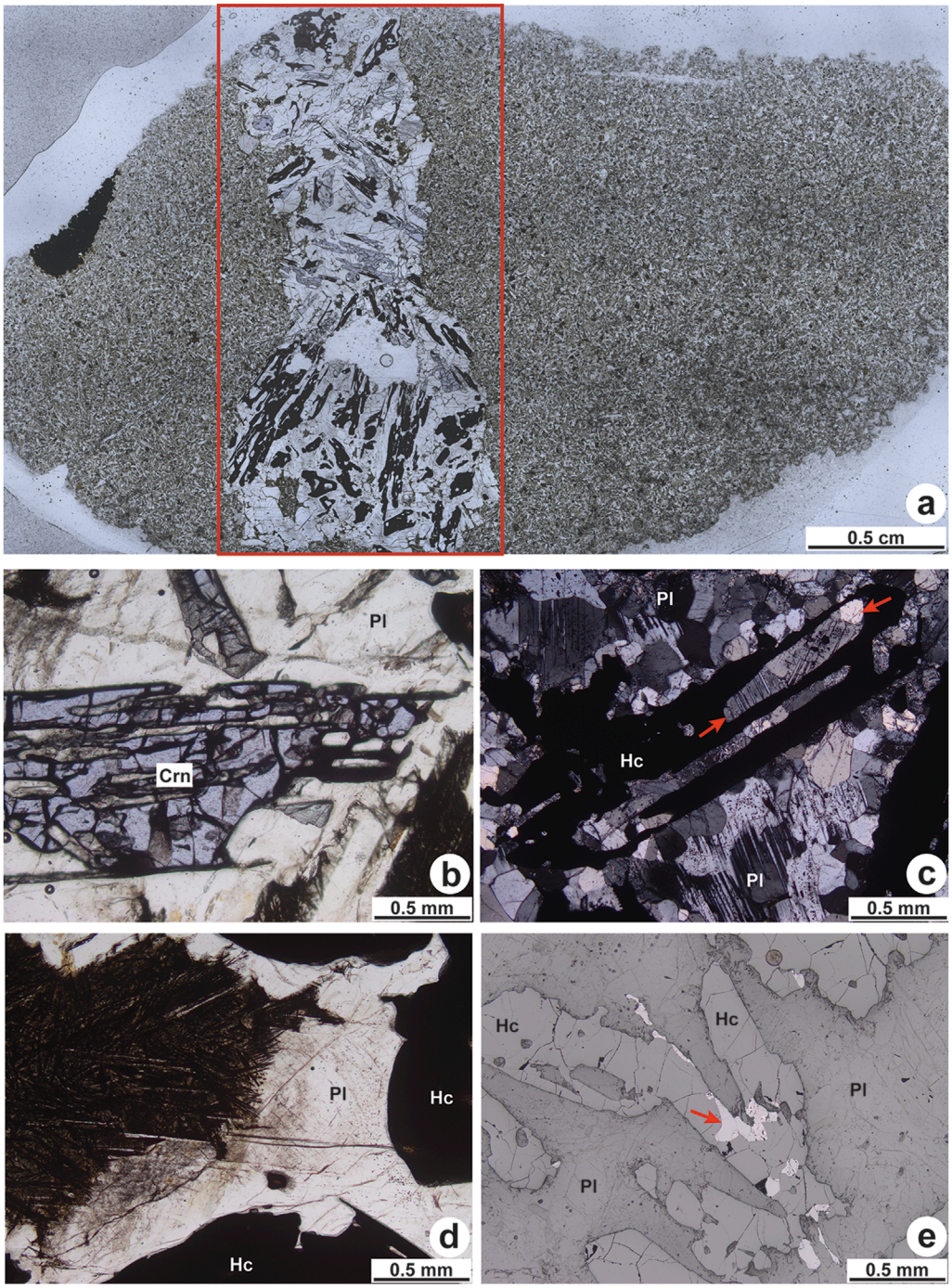

FIGURE 4
Photomicrographs of Rudh' a' Chromain sample Mu-B-4. **(a)** Scan of the thin section studied, showing an irregularly-shaped xenolith contained in the relatively fine-grained groundmass of the sill. The area examined in detail is demarcated by the red rectangle. **(b)** Plane-polarised light image of skeletal corundum crystal set in oikocrystic plagioclase. **(c)** Cross-polarised light image of skeletal hercynite crystal set in a groundmass of relatively fine-grained subhedral plagioclase. Note the elongate inclusion of plagioclase in the hercynite (arrowed), itself comprising three crystals of plagioclase, none of which are in optical continuity with the plagioclase in the groundmass. **(d)** Plane-polarised light photomicrograph of a pocket of densely intergrown mullite needles, presumably set in brownish-coloured devitrified glass. The white mineral is a relatively large plagioclase oikocryst, and the opaque crystals are hercynite. **(e)** Reflected light image of skeletal hercynite crystals. Note the relatively high reflectance phase (arrowed) intergrown with the hercynite in such a way that the shape of the crystal appears unmodified. This bright phase is ilmenite. Mineral abbreviations as for Figure 3.

grain was used to calculate an orientation density function (ODF), which is then plotted on equal area, lower hemisphere stereoplots. The ODF values were calculated using a 10° halfwidth. As feldspar crystals are twinned, their ODF values were calculated using every measurement available as one point per grain representations are not suitable.

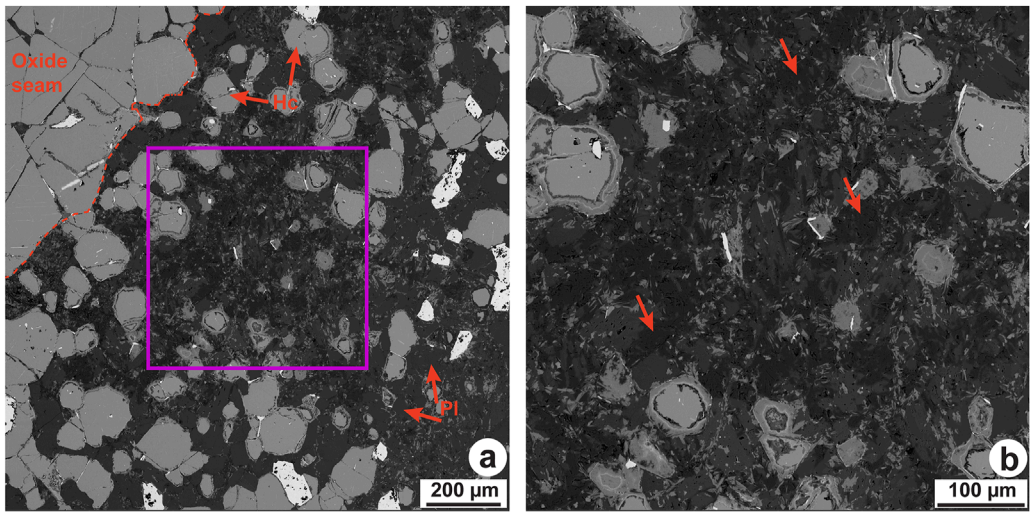

FIGURE 5
Backscattered electron images illustrating an amorphous or fine-grained portion of Ard-B-2. The location of panel **(a)** is shown in Figure 3a, and the purple outline box shows the position of panel **(b)**. The position of an oxide seam is highlighted in the top left. The red arrows in **(b)** highlight examples of dark-coloured amorphous material, that is interpreted here to have originally been glass. Mineral abbreviations as for Figure 3. See text for further discussion.

To check for crystallographic relationships between phases, crystallographic orientations were extracted at two pixels at the grain boundaries between two selected grains from different phases. Mineral orientations are then displayed in sets of pole figures showing correspondences between the axis and planes of interest for the mineral phases in question. For each combination of axes, the minimum angle between the closest two orientations, including symmetry, was calculated.

Results

Backscattered electron imaging and mineral compositions

Backscattered electron images of representative areas containing the fine-grained or amorphous regions in Ard-B-2 are shown in Figure 5. Energy-dispersive X-ray spectra (EDS) points on several of the darker-coloured (amorphous) regions shown in this image and others like it indicate they are relatively Al- and Si-rich.

Summary plots of the mineral chemical variations observed in Ard-B-2 and Mu-B-4 are presented in Figure 6, and the full datasets are tabulated in the electronic supplement. In general, we do not see significant variation in mineral chemistry with microstructural position, within each sample. Corundum Al_2O_3 concentrations for Ard-B-2 range from ~95–100 wt% (Figure 6a). Where Al_2O_3 is lower, FeO is generally higher, with concentrations of up to ~4 wt% measured for the analysis with the lowest Al_2O_3 (Figures 6a,b). Measurable amounts of TiO_2 are also observed, with an average of 0.23 wt% (n = 28) for all points in Ard-B-2. Corundum in Mu-B-4 exhibits higher and much more consistent Al_2O_3 (always between 99–100 wt%; n = 17), with measurable FeO (average of 0.61 wt%; n = 17) and TiO_2 (average of 0.21 wt%; n = 17) observed (Figures 6a,b). No correlation between Al_2O_3 and FeO or TiO_2 is observed in Mu-B-4.

The main spinel phase in Ard-B-2 is close to end-member hercynite in composition, with only a small amount of MgO (average of 2.51 wt%; n = 71) present. Higher MgO (and lower FeO) is observed in hercynite distributed in the plagioclase-rich portions of the sample, compared to hercynite in the hercynite-rich parts. The only other elements consistently present (in trace quantities) are V_2O_3 (average of 0.15 wt%; n = 71) and MnO (average of 0.15 wt%; n = 71). Using the technique of Droop (1987) and assuming stoichiometry, we calculated the average $Fe^{3+}/\Sigma Fe$ ratio of the Ard-B-2 hercynites as 0.17 ± 0.02 (n = 71), corresponding to an average Fe_2O_3 content of 8.0 ± 0.8 wt%. Of the different textural types of hercynite analysed in Ard-B-2, including coarse-grained crystals in the largest seams, finer-grained crystals in small seams, and disseminated within the plagioclase-rich portions of the sample, no convincing compositional differences were observed. The spinel in Mu-B-4 has spinel and hercynite components present in approximately equal proportions. No systematic variation in hercynite composition is observed in one part of the xenolith or another. The hercynite has relatively high TiO_2 (average of 0.45 wt%; n = 22) and trace quantities of Cr_2O_3 and MnO (≤0.18 wt% and ≤0.3 wt%, respectively). The average $Fe^{3+}/\Sigma Fe$ ratio of the Mu-B-4 hercynite is 0.06 ± 0.02 (n = 22), with an average Fe_2O_3 content of 1.4 ± 0.5. Hercynite from both Ard-B-2 and Mu-B-4 shows well developed negative correlations between Al and Fe^{3+}# ($Fe^{3+}/[Fe^{3+}+Fe^{2+}]$; Figure 6c), albeit displaced to higher Al and lower Fe^{3+} contents in the case of the latter.

Ilmenite is relatively abundant (~10 mod.%) in Ard-B-2 and exhibits an almost ideal endmember composition. It consistently contains trace amounts of MnO (average of 0.27 ± 0.05; n = 56) and V_2O_3, the latter usually above or just above detection limits. Values for Fe^{3+}# in Ard-B-2 average 0.05 ± 0.02 (n = 50),

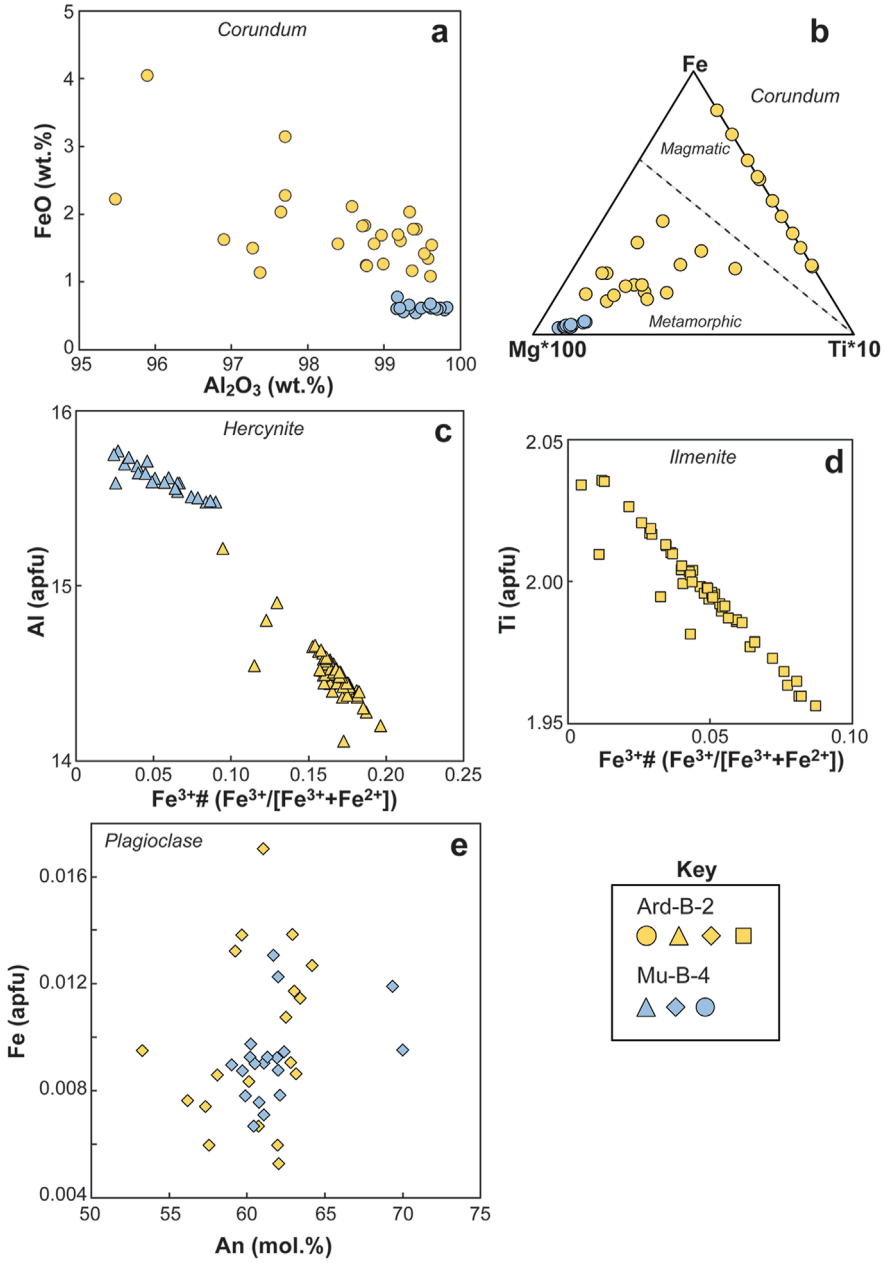

FIGURE 6
Mineral chemical data collected by electron microprobe for various phases of the Glebe Hill and Rudh' a' Chromain samples. **(a)** Corundum FeO versus Al_2O_3. **(b)** Ternary (Fe-Ti*10-Mg*100) diagram showing the variation in corundum composition for both samples. The magmatic and metamorphic fields for corundum are shown for reference and are taken from Voudouris et al. (2019). **(c)** Al (apfu) versus Fe^{3+}# (Fe^{3+}/[Fe^{3+}+Fe^{2+}]) in hercynite. **(d)** Ilmenite Ti (apfu) concentration versus Fe^{3+}# (Fe^{3+}/[Fe^{3+}+Fe^{2+}]). Note that ilmenite in Mu-B-4 did not contain resolvable Fe^{3+}. **(e)** Plagioclase Fe (apfu) versus An (mol%) content. Inset shows the key for the symbols for each panel.

and the range of Fe^{3+}# versus Ti (apfu) is shown in Figure 6d. Ilmenite CaO is relatively high (up to ~0.3 wt%) when associated with coarse-grained plagioclase, in small (1–2 mm thick) hercynite clusters. We only analysed four ilmenite grains from Mu-B-4 – these are much more variable in composition than those in Ard-B-2, with several wt% of both Al_2O_3 and MgO typically present. Ferric iron concentrations in these ilmenites are not resolvable. One grain of rutile was also analysed, with close to endmember TiO_2 composition.

Plagioclase compositions in Ard-B-2 span a range of An_{53-64} mol% and FeO of 0.22–0.72 wt% (n = 19; Figure 6e). The TiO_2 concentrations are consistently above detection limits (average of 0.14 ± 0.02). Of the various textural types of plagioclase analysed in Ard-B-2 (*i.e.*, fine-grained, coarse-grained, association with hercynite seams or not), no consistent pattern was observed between microstructure and mineral chemistry. We did not separately analyse cores and rims of any of the sparse optically-zoned plagioclase, so are unable to verify if this

texture corresponds to significant chemical zonation. Plagioclase in Mu-B-4 reveals a compositional range of An_{59-70} and FeO of 0.28–0.55 wt% (n = 19; Figure 6e). Its average TiO_2 content is 0.18 ± 0.04. Again, no consistent mineral chemical differences are observed based on microstructure (*i.e.*, from one part of the xenolith to another or in large oikocrystic plagioclase versus fine-grained crystals).

Electron backscatter diffraction results

Ard-B-2

The EBSD data for Ard-B-2 are illustrated in Figures 7, 8. The main minerals studied (corundum, hercynite, ilmenite and plagioclase) can be clearly distinguished on the basis of their microstructure, as well as their crystallographic and diffraction characteristics. The fine-grained and amorphous areas of the sample did not index as they do not bear any reflective planes. The mean orientation maps for hercynite indicate the seams comprise granular aggregates of randomly oriented grains. Similarly, no preferred orientation is observed for finer-grained hercynite within the plagioclase-rich portions of the rock. The mean orientation maps for the ilmenite reveal that it forms relatively large oikocrysts within the seams, filling the porosity between hercynite crystals (Figure 7a). Thus, much of the ilmenite in a given seam comprises one or two relatively large crystals. Finer-grained ilmenite in the plagioclase-rich portion of the rock shows no preferred orientation.

The high resolution EBSD mapping shows that, in addition to its occurrence in the seams, relatively fine-grained corundum is sparsely distributed throughout the plagioclase-rich portion of the rock. These maps also show that corundum is intimately associated with ilmenite within and at the margins of the spinel-rich portions of the sample, such that ilmenite crystals typically exhibit μm-sized corundum crystals as inclusions and along ilmenite-hercynite grain boundaries (Figure 7b). A close relationship between corundum and ilmenite crystal orientations is strongly suggested at the thin section scale by the pole figures for these minerals which show clear clustering and common orientation for the [0001] axes of both minerals (Figures 7c,d). Although more weakly-developed, the pole figures also suggest a crystallographic relationship between the $[10\bar{1}0]$ axes for both minerals, which share similar secondary maxima.

In order to investigate the corundum-ilmenite relationship more closely, we analysed the interfaces between several specific pairs of crystals, including relatively large crystals of each phase in contact with one another and also corundum inclusions within ilmenite. The axes of interest for both phases are then plotted in the same space. In particular, we examined the relationship between (0001) and $(10\bar{1}0)$ for each of the corundum and ilmenite pairs (see Figures 7e,f). In all cases, the resulting relationships strongly suggest that corundum and ilmenite share a common orientation for (0001) but also for their crystal facets. In repeating the exercise for corundum-hercynite pairs, where hercynite [100], [111] and [110] are compared to the same two corundum elements, clear crystallographic relationships are not observed. One exception is hercynite [110], where there is a suggestion that this axis is oriented similarly to some corundum crystal faces.

For the plagioclase-rich portion of Ard-B-2, the EBSD data highlight the main observation from petrography, which is that plagioclase grain size is typically relatively small except in close proximity to hercynite-rich seams or the fine-grained and amorphous areas that line seam edges (Figure 8a). It is also evident that plagioclase is completely absent from the hercynite-rich parts of the sample. The EBSD data also reveal a weak but very consistent crystallographic fabric: the pole figure for plagioclase shows a clustering of [010] axes as well as well-developed point maxima for [001] and [100] (Figure 8b). The 2 μm step size map shows that this fabric is represented in subsets of the sample volume, as well as at the thin section scale. The data also indicate a relatively high density of twin interfaces in plagioclase, and show that the twin populations are dominated by Albite, Carlsbad-A and Albite-Carlsbad-A twinning, with a subsidiary population of Pericline and Ala-B twinning (Figures 8c,d). We note that Carlsbad-A and Albite-Carlsbad-A twinned plagioclase grains have strongly oriented [010] and [001] axes, whereas the subset of crystals with albite twins or grains that appear untwinned have a well-developed clustering of [100] axes and girdles for [010] and [001].

Mu-B-4

The EBSD data for this sample are illustrated in Figures 9–11. The main minerals studied (corundum, hercynite and plagioclase) indexed relatively well and only a minor proportion of the sample, mainly comprising relatively small irregularly-shaped zones of alteration in the groundmass, as well a larger area of missing sample on the thin section within the xenolith, was not analysed. The EBSD mapping clearly shows the corundum-dominated part of the xenolith is largely comprised of one relatively coarse-grained oikocryst (Figure 9a), whereas the hercynite-dominated part is composed of many more finer-grained plagioclase crystals that are not oikocrystic. The pole figure for plagioclase in the xenolith illustrates well-developed point maxima for [100], [010] and [001], although clustering of these axes occurs in other subsidiary orientations as well (Figure 9b). Each cluster in the latter plot comprises a single plagioclase oikocryst that is overrepresented because of the ODF calculation method. Plagioclase in the groundmass does not show well developed point maxima (Figure 9c). In the large oikocryst, tapered twins at the crystal margins are truncated at the xenolith margins. Fine-grained plagioclase is one of the most abundant phases in the host rock and does not appear to show a preferred orientation. In the xenolith, plagioclase twin populations are dominated by albite (10.5 cm^{-1}) and pericline (6.7 cm^{-1}). The host rock (*i.e.*, the sill groundmass material) has a different plagioclase twin law density distribution with Albite (9 cm^{-1}), Carlsbad-A (6.7 cm^{-1}), Pericline (1.2 cm^{-1}) and traces of Ala-B and Albite-Carlsbad-A twins.

The mean orientation map for the skeletal corundum illustrates it occurs as randomly oriented single crystals (Figure 10a). However, the hercynite pseudomorphing the corundum comprises aggregates of apparently randomly (crystallographically) oriented granular crystals (Figure 10b). In the corundum-dominated part of the xenolith, where hercynite is sparse, it is seen that despite comprising multiple crystals, hercynite perfectly pseudomorphs the corundum. As for Ard-B-2, we investigated the corundum-hercynite relationship more closely by analysing the interfaces between 13 specific pairs of crystals (Figures 11a,b). Again, the relationship

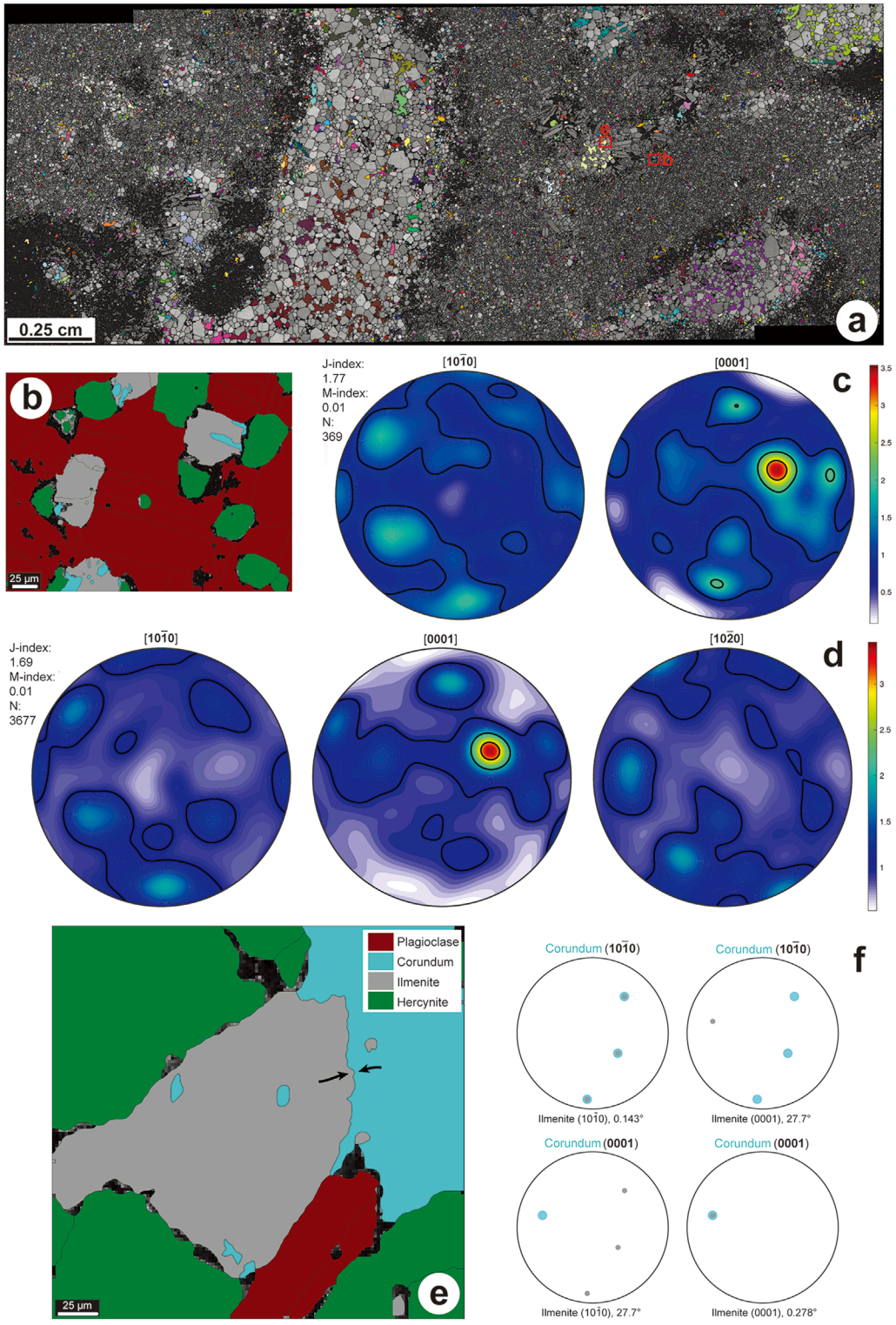

FIGURE 7
Electron backscatter diffraction results for ilmenite and corundum in Ard-B-2. **(a)** Mean orientation map for ilmenite in entire sample area. The area covered is the same as that highlighted by the red rectangle in Figure 3a. The locations of **(b,e)** are shown by the red outline boxes. **(b)** Phase map of hercynite (green), plagioclase (red), ilmenite (grey) and corundum (cyan). Note the intergrowths and inclusions of corundum within the ilmenite grains. **(c,d)** Pole figures for corundum and ilmenite, respectively. **(e,f)** Detailed investigation of crystallographic relationship between ilmenite and corundum (see text for discussion). The black arrows indicate the positions of the points taken for comparison in each phase.

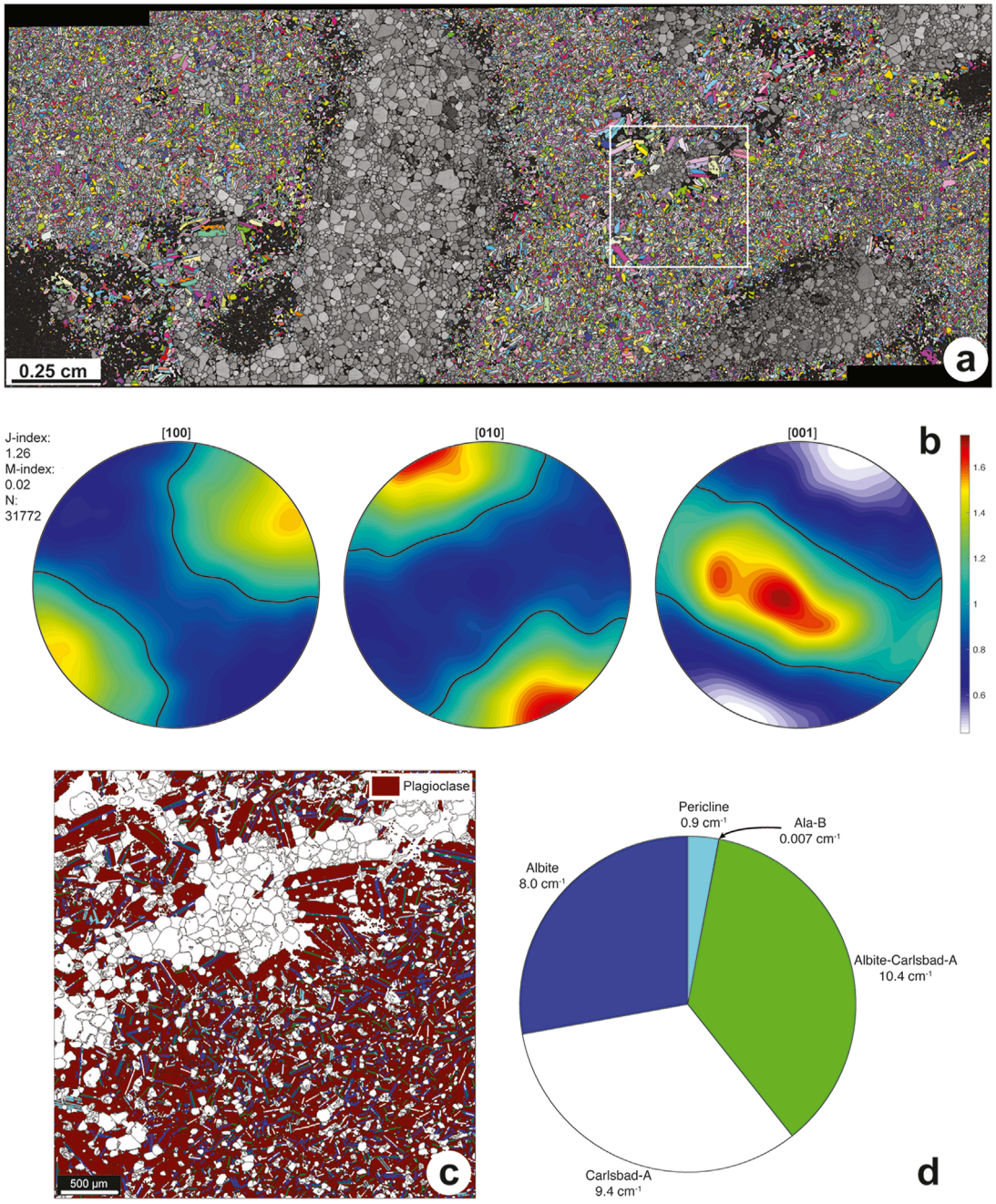

FIGURE 8
Electron backscatter diffraction results for plagioclase in Ard-B-2. **(a)** Mean orientation map for plagioclase in entire sample area. The area covered is the same as that highlighted by the red rectangle in Figure 3a. The white outline box shows the location of panel **(c)**. **(b)** Pole figures for plagioclase crystallographic axes. **(c)** Map of the distribution of plagioclase twin laws in a portion of the studied sample. **(d)** Pie chart showing the relative proportions of plagioclase twin laws in Ard-B-2, in which the interface lengths for each twin law are reported. The interface lengths are reported and normalised to the surface area to give an interface density in cm^{-1}.

between the corundum facets and each of hercynite [100], [111] and [110] was examined, and the exercise repeated for corundum (0001) with hercynite [100], [111] and [110]. The results show that three hercynite [110] axes are often oriented closely to the three corundum crystal faces (Figure 11b; 7/13 < 12°, with a minimum angle of 2.63°). Similarly, a subset (4/13) of interfaces show hercynite [111] lies close to corundum (0001) (Figure 11b). Maps of the misorientation to the mean grain orientation show that the hercynite aggregates comprise two types of grains: (1) relatively large grains with internal misorientation and mostly concave grain boundaries and (2) smaller grains free of internal misorientation, texturally equilibrated with each other and exhibiting convex grain boundaries with the other hercynite population. It is notable that the coarse-grained hercynite tends to occur in regions of particularly small plagioclase grain size.

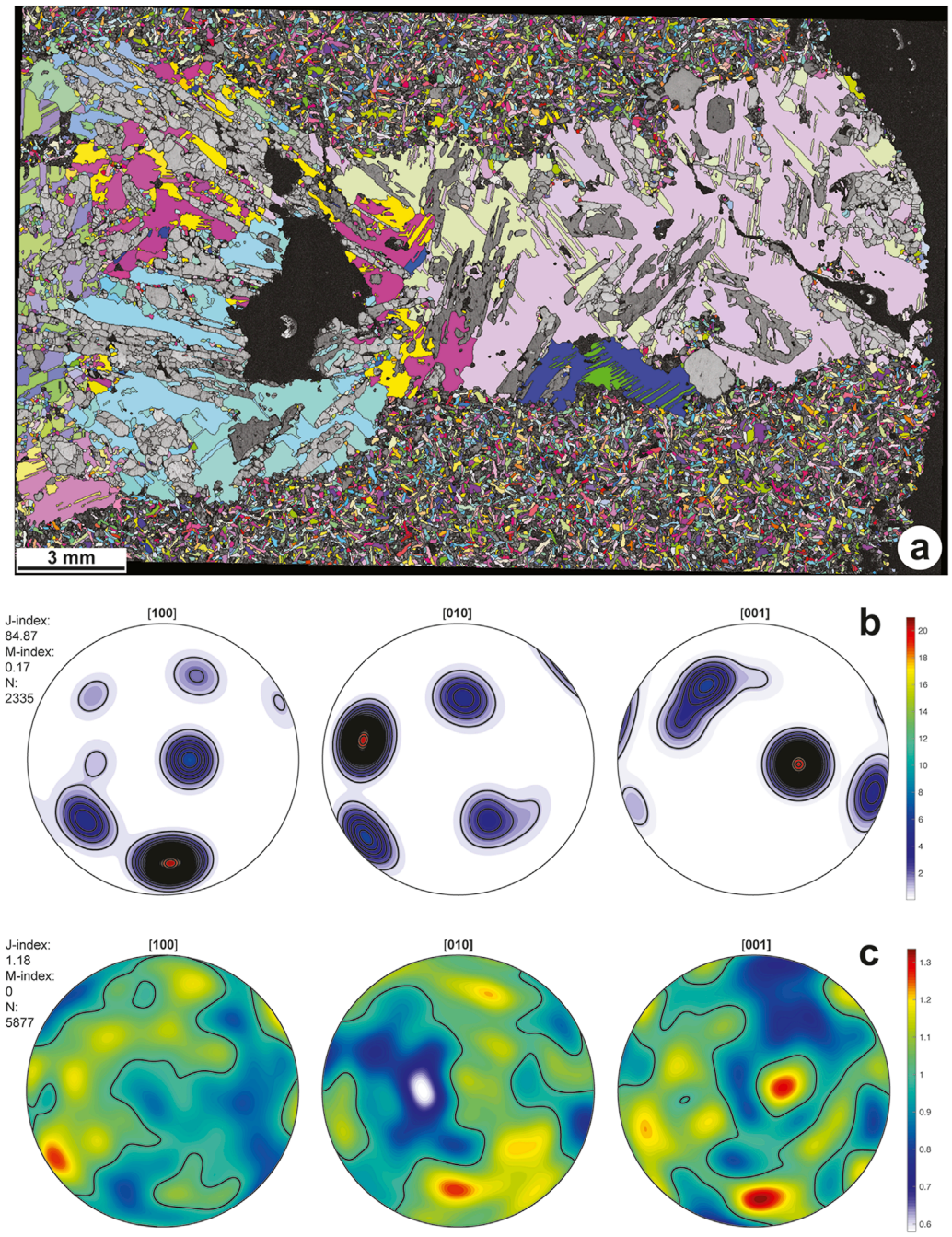

FIGURE 9
Electron backscatter diffraction results for plagioclase in Mu-B-4. **(a)** Mean orientation map for plagioclase in entire sample area. The area displayed is approximately that highlighted by the red rectangle in Figure 4a. **(b)** Pole figures for plagioclase crystallographic axes within the xenolith studied. **(c)** Pole figures for plagioclase crystallographic axes for the Mu-B-4 groundmass, *i.e.*, all plagioclase outside of the xenolith margins.

As with plagioclase, fine-grained diopside in the groundmass exhibits no discernible orientation. Hercynite is relatively abundant and evenly distributed in the groundmass, as small (<10 μm) sized equant crystals. Ilmenite, for which a small number of grains are observed in the xenolith, is not present in the groundmass. Calcite, present as relatively large (several mm sized) randomly oriented crystals attached to the margins of the xenolith, is also distributed throughout the groundmass as much finer grained (<50 μm) crystals.

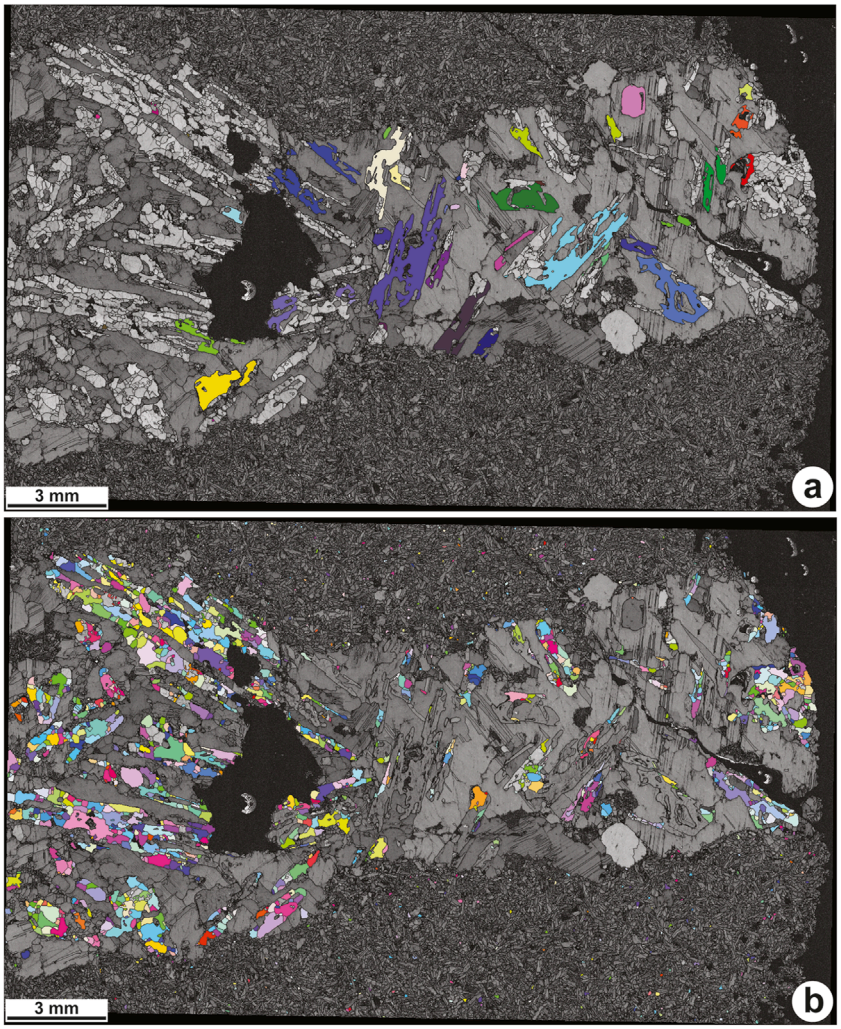

FIGURE 10
Electron backscatter diffraction results for corundum and hercynite in Mu-B-4. **(a)** Mean orientation map for corundum in entire sample area. **(b)** Mean orientation map for hercynite over entire sample area. The area displayed in panels a and b is approximately that highlighted by the red rectangle in Figure 4a.

Discussion

A liquid immiscibility origin for the Glebe Hill corundum-bearing assemblage?

The Glebe Hill assemblage has not been studied in detail for almost a century (Richey and Thomas, 1930). On the basis of their field and petrographic observations, the latter authors suggested the bulk chemistry of the rock was unchanged from its protolith, *i.e.*, there was no evidence for mixing or mingling with the magmas that crystallised the surrounding gabbros. Richey and Thomas (1930) highlighted the lack of any aluminous sedimentary rocks proximal to the Glebe Hill locality and suggested instead that a weathered basaltic rock (*i.e.*, bole) might have provided the necessary Fe and Al to produce the quantities of plagioclase and oxide observed. Subsequent studies that examined the Glebe Hill rocks have not seriously contested this interpretation (*e.g.*, Wells, 1951), though the latter noted a variety of other types of Al-rich metasedimentary xenoliths included elsewhere in the Hypersthene Gabbro for which a Fe-rich (bole) composition is not suitable as a protolith. Day (1989), citing the field observations of Richey and Thomas (1930), noted the presence of a thin sequence of Paleogene sedimentary rocks (including mudstones, ironstones, lignite and altered basaltic tuff) in another part of the Ardnamurchan peninsula and suggested that such a protolith might also explain the Glebe Hill assemblage. The metamorphism of laterite (including bauxite) is now generally understood to result in a rock mainly composed of corundum + spinel + magnetite (*i.e.*, emery; Grapes, 2011), so the complete lack of magnetite in Ard-B-2 does not appear to support the original interpretation of a lateritic soil protolith. The Paleogene mudstones referred to by Day (1989) are rich in organic material, and together with this observation, Day (1989) used ilmenite Fe^{3+} contents to suggest a range of $-\log fO_2$ of −7 to −19 at 1,100°C, after Turnock and Eugster (1962). Our calculated hercynite Fe_2O_3 contents (average 8.0 ± 0.8 wt%; 1σ SD; n = 71; using Droop, 1987) are similar to those reported by Day (1989), so we are inclined

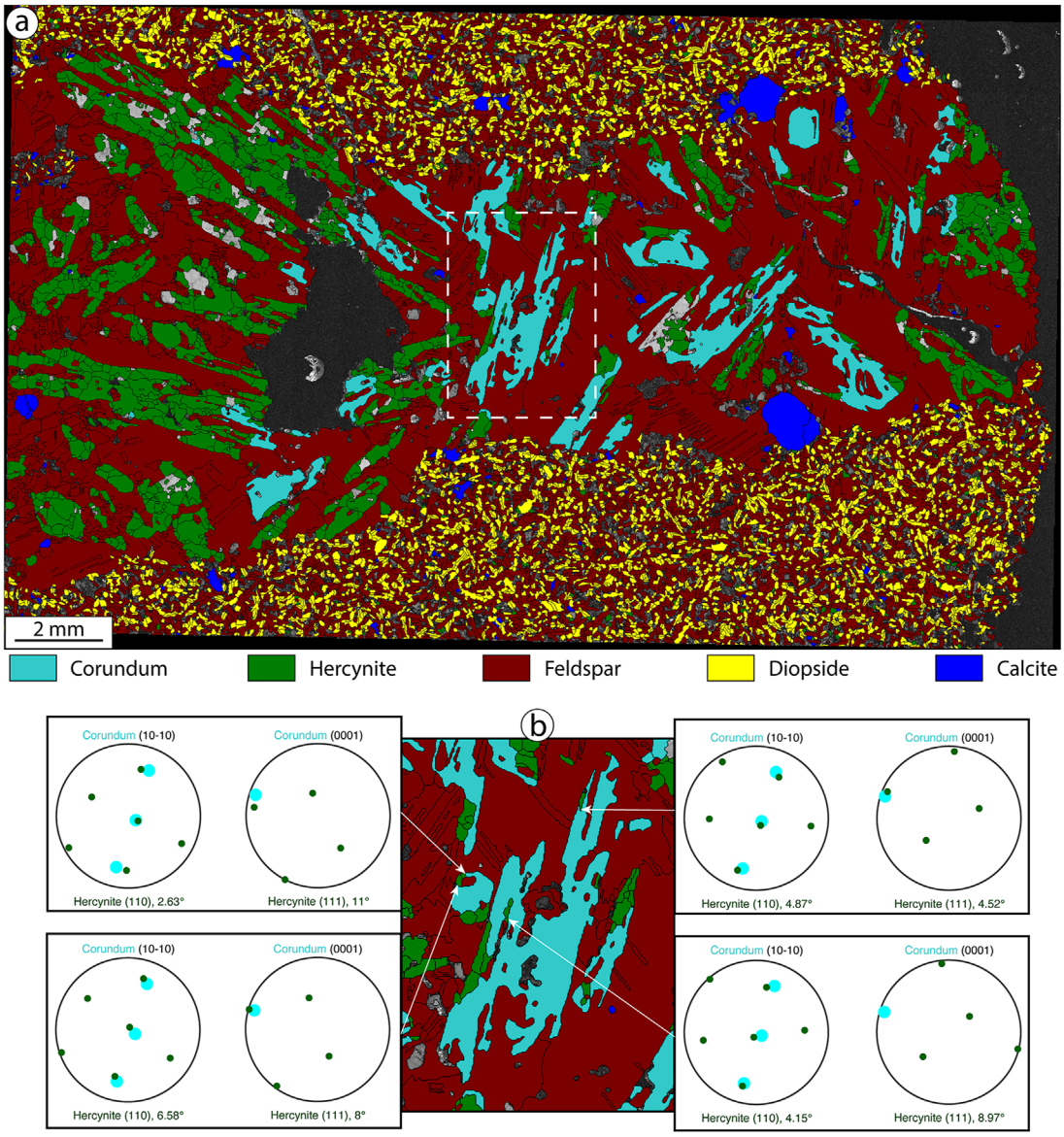

FIGURE 11
Electron backscatter diffraction results for corundum and hercynite in Mu-B-4. **(a)** Phase map for Mu-B-4, with plagioclase in red, diopside in yellow, hercynite in green, corundum in cyan and calcite in blue. The rectangle in dashed white highlights an area in which detailed examination of the crystallographic relationship between the hercynite shown in **(b)**. **(b)** Results of the examination of the crystallographic relationship between hercynite and corundum at the interface of 4 different couples of grains, indicated by the white arrows. See text for discussion.

to agree that Ard-B-2 formed under relatively reducing conditions (Figure 12). We additionally estimated the fO_2 of the system using the oxybarometer of Zhao et al. (1999), assuming pressures of 1 kbar and 1,100°C, and obtained values of $-\log fO_2$ of −10.8 ± 1.0 (1σ SD; n = 32). These are upper estimates only, because rutile was not observed in these rocks, but fall within the range of values suggested by Day (1989).

Regardless of the protolith and precise temperature-fO_2 conditions of formation of the Glebe Hill assemblage, the formation of distinct highly irregularly-shaped and distributed plagioclase and spinel-rich domains in the rock is, in our view, one of the key factors in interpreting its petrogenesis. An important observation from the EBSD data is that the interstitial parts of most of the hercynite-rich domains contain a single large ilmenite oikocryst, the latter lacking evidence for internal misorientation. Together with the low apparent hercynite-hercynite-ilmenite dihedral angles, this strongly suggests that the ilmenite pseudomorphs an intercumulus melt phase (see Duchesne, 1996). There is no plagioclase in the hercynite-rich portions of the rock, but pockets of fine-grained and amorphous material occur interstitially and it is generally in these areas where corundum is most common and has the largest grain sizes. Richey and Thomas (1930) interpreted these areas as devitrified glass and we concur with this observation. The well-developed crystallographic relationship between corundum and ilmenite observed in the EBSD

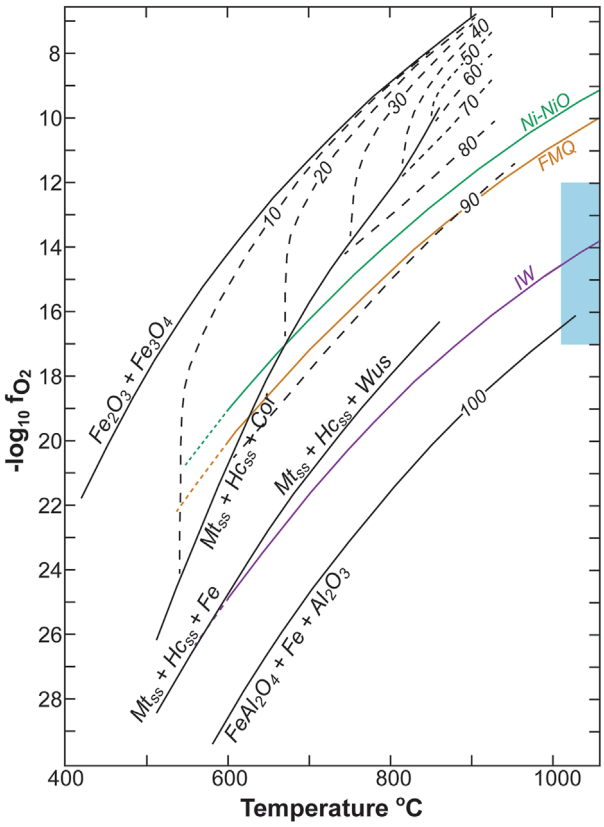

FIGURE 12
Oxygen fugacity (log) versus temperature plot redrawn from Turnock and Eugster (1962), showing various spinels that may coexist with corundum. The dashed numbered lines are composition contours of magnetite-hercynite solid solution at 10 mol% $FeAl_2O_4$ increments. Also shown are curves for common buffer assemblages (IW, iron-wustite; FMQ, fayalite-magnetite-quartz; Ni-NiO, nickel-nickel oxide) from Frost (1991). The blue-filled box marks the approximate region suggested by Day (1989) for crystallisation of the Glebe Hill assemblage.

data, together with the observation that these phases are locally intimately intergrown with one another, indicates a replacement reaction, and the combined petrographic and EBSD information strongly suggests that ilmenite growth postdates that of corundum. Although much less well defined, the EBSD hint at a relationship between hercynite and corundum too, with hercynite [110] oriented similarly to certain corundum faces. The development of a relatively coarse-grained polygonal texture in hercynite, with hercynite-hercynite-hercynite apparent dihedral angles typically at ~120°, suggests textural equilibration via Ostwald ripening at subsolidus temperatures within the interiors of the spinel-rich portions of the sample.

In the plagioclase-rich domains of the rock, minor hercynite, corundum and ilmenite occur, mainly in the interstices between plagioclase crystals. Even though sparse in abundance, where corundum crystals are observed they are always close to (or touching) an ilmenite crystal. An exception is where inclusions of hercynite are distributed within some plagioclase crystals in a manner pointing to concentration within specific growth zones. This suggests that plagioclase and hercynite formed early, and that corundum and ilmenite crystallisation in these domains occurred later. A number of key observations indicate that the plagioclase textures are magmatic. One is the presence of relatively common, albeit not ubiquitous, compositional zoning in plagioclase throughout the rock. Another is the generally euhedral morphology of the plagioclase, pointing to relatively high melt-rock ratios during fabric formation. The nature of the plagioclase twin plane populations in Ard-B-2 are also informative; these are dominated by Carlsbad-A and Albite-Carlsbad-A twins, normally considered to be a product of magmatic growth (*e.g.*, Winchell, 1951; Smith, 2013). In addition, no evidence for subsolidus intracrystalline misorientation in plagioclase is observed. The largest euhedral plagioclase crystals occur close to the boundaries with hercynite-rich domains, which are also always areas that contain pockets of fine-grained or amorphous material. The EBSD data indicate that plagioclase throughout Ard-B-2 carries a weak but pervasive orthorhombic fabric with relatively stronger point maxima for [010] and [001] (Figure 8b). Together with the field aspect of the rock, which has the appearance of having been mobile in a mushy state (*e.g.*, the chaotic and disturbed nature of the spinel-plagioclase layering; Figure 2a), the nature of this EBSD fabric is best explained as a result of magmatic processes (*i.e.*, with [010] and [001] being involved in the formation of the magmatic fabrics; see Satsukawa et al., 2013; Holness et al., 2017 for similar examples), possibly synchronous with plagioclase growth, rather than deformation in the solid state. The combined evidence thus points to processes operating within a crystal mush, with sufficient melt present to facilitate concomitant plagioclase growth and prevent viscous deformation (per the definition of the latter used by Holness et al., 2017).

The combined observations for both the hercynite- and plagioclase-rich portions of the Glebe Hill assemblage therefore suggest a magmatic origin in terms of crystallisation of the minerals. Unlike the xenoliths described by Markl (2005), it is not clear that the rocks represented by Ard-B-2 reflect a second iteration of melting. The latter study discussed the formation of a viscous, H_2O-poor Al-rich melt from refractory residues incorporated into the Skaergaard intrusion, after granitic melt had already been extracted from the original protolith. It was within this Al-rich melt that corundum, plagioclase and hercynite were considered to have grown. Day (1989) did map numerous thin (<0.5 m) felsic sheet intrusions in close proximity to the Glebe Hill locality, that could represent escaped granitic melts. However, although aluminous too, the high ferrous iron content of Ard-B-2 necessitates consideration of a composition beyond that of a pelitic protolith. Using the compositions and modal proportions of the main minerals (plagioclase, hercynite, ilmenite and corundum), we calculated an approximate bulk rock chemistry for the Glebe Hill material and modelled the equilibrium assemblages produced between 300°C–1,300°C, at 1 kbar, using the Theriak-Domino software suite (Figure 13a; JUN92d database; de Capitani and Brown, 1987; de Capitani and Petrakakis, 2010). The proportions of the phases are relatively consistent over this temperature range and reflect those of Ard-B-2 fairly well, particularly at the higher temperature end of the range that we consider the corundum-anorthite-hercynite assemblage to have formed at (*i.e.*, 1,000°C–1,100°C; see also Day, 1989). Components represented by the predicted (small) proportions of olivine and nepheline at these temperatures could also be taken up by the pockets of (now devitrified) glassy material in

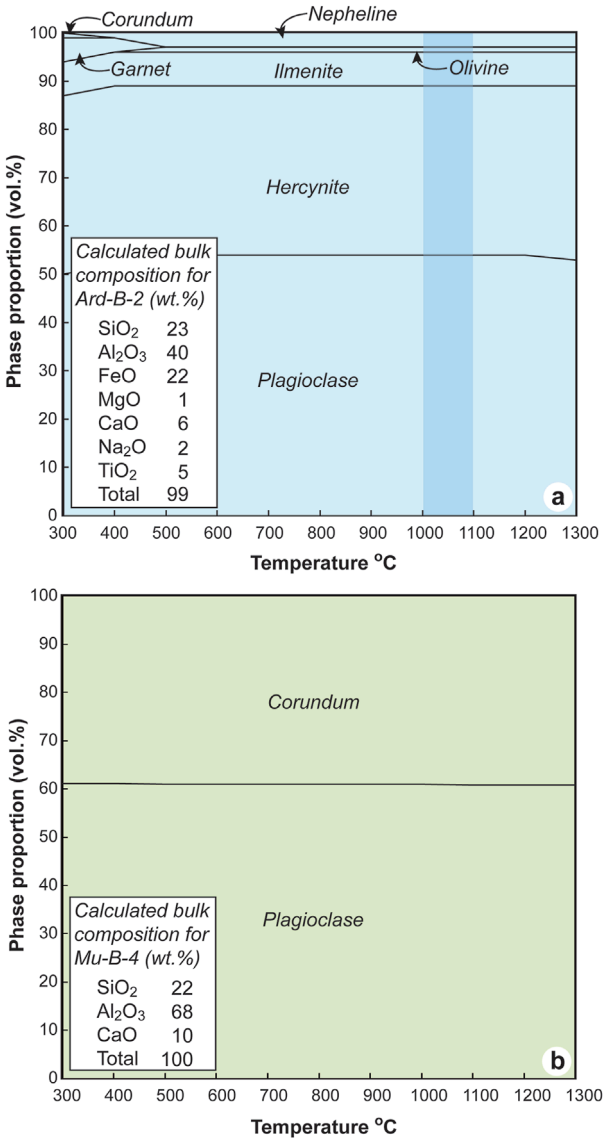

FIGURE 13
(a) Plot of proportions of phases versus temperature for an estimated bulk composition of **(a)** Ard-B-2 and **(b)** Mu-B-2, in both cases based on mineral compositions and observed mineral proportions and shown in the bottom left of each panel. The vertical darker blue bar in **(a)** is the suggested temperature of formation of Ard-B-2 (see also Day, 1989). The equilibrium assemblages were calculated in Theriak-Domino using the JUN92d.bs database. The black lines defining the fields are extrapolated between temperature points.

the rock. The modelled scenario would have required the protolith to have 40 wt% Al_2O_3 and 22 wt% FeO (see Figure 13a for bulk composition used). While these FeO contents are not dissimilar to those of ironstones in the vicinity, Al_2O_3 contents of this magnitude are harder to rationalise in an unmodified sedimentary rock. Therefore, we consider the ~1 m sedimentary package of lignite, ironstone and mudstone that locally occurs on Ardnamurchan to be a reasonable precursor for the Glebe Hill assemblage (Day, 1989), with some loss of a felsic melt component possibly having occurred first.

The microstructures of both hercynite- and plagioclase-rich portions of the rock are unequivocally magmatic, leading us to further suggest, principally on the basis of these textures, the possibility that the Glebe Hill rocks formed as a result of the development of immiscible Al- and Fe-rich melts. As melts, the Fe-rich variant would have been less viscous, and could have accumulated more easily in the domains now rich in hercynite, whereas the plagioclase laths carried in the more viscous Al-rich melt acquired a preferred orientation during flow of the crystal mush and trapped ilmenite, hercynite and corundum in the interstices of plagioclase crystals. Liquid immiscibility has been found to be more effective as a process under sustained high temperature (Lino et al., 2023) and higher oxygen fugacity (Naslund, 1983), but perhaps the unusual composition of the Ard-B-2 promoted the segregation of the two components. In any case, the suggestion of Richey and Thomas (1930) that the original protolith for the Glebe Hill rocks was a laterite seems not to be tenable, because of the absence of magnetite. Instead, we concur with Day (1989), that high-temperature metamorphism of the package of Paleogene sedimentary units would have led to melting under relatively reducing conditions, as well as the production of abundant hercynite.

The pockets of devitrified glassy material in Ard-B-2 probably represent pseudomorphed residual Al-rich melt. Where these occur within or around the edges of the hercynite-rich portions of the rock, they may reflect occlusion as a result of melt immiscibility. They are typically the sites of early corundum growth, which probably occurred simultaneously with hercynite, but due to either pore-scale differentiation of these interstitial melts or their reaction with hercynite, or both, ilmenite grew as a late phase at the expense of corundum. The fact that hercynite, corundum and ilmenite occur disseminated throughout the plagioclase-rich portions of the rock suggests that this process occurred interstitially to the plagioclase framework as well. The covariation of hercynite Al and Fe^{3+} contents may reflect interstitial melt differentiation in both portions of the rock, implying the presence of crystal-scale variations in fO_2 in the trapped melt fraction. The local coarsening of euhedral plagioclase crystals against the devitrified glassy material points to the growth of the plagioclase into a melt phase.

Multi-stage melt-xenolith reaction in the Rudh' a' Chromain sill

In contrast to the Glebe Hill assemblage, the Rudh' a' Chromain xenoliths resemble other corundum-anorthite-spinel assemblages described in the literature more closely, particularly in terms of the relative proportions of the main minerals (Preston et al., 1999; Markl, 2005; Mariga et al., 2006a; Mariga et al., 2006b). At Rudh a' Chromain, it has been observed that the corundum-anorthite-spinel paragenesis generally occurs as rims around mullite buchite cores. Such a relationship has been used to propose that the rims form as a result of an iterative melting process, with corundum-anorthite-spinel crystallising in molten refractory residues that have experienced some (granitic) melt loss already. While certain details change (*e.g.*, the absence of buchite in the Skaergaard xenoliths described by Markl, 2005), this iterative process of formation appears key to forming the assemblage. A

striking similarity is present between the partly pseudomorphed corundum dendrites described by Mariga et al. (2006a) and those in Mu-B-4. In the Mariga et al. (2006a) study, constant volume replacement, possibly as a consequence of invading mafic melt from the xenolith host, were invoked to explain the texture observed, via the following reaction (Equation 1):

$$\text{Corundum} + \text{Melt 1} = \text{Hercynite} + \text{Melt 2} \quad (1)$$

Markl (2005) outlined a five stage process in the formation of the xenoliths associated with the Skaergaard intrusion and noted that typical corundum-bearing xenoliths are zoned, with corundum-plagioclase-spinel-bearing cores, overgrown by plagioclase-spinel-bearing mantles, rimmed in turn by an outer layer of anorthosite. This structure bears strong similarities to the structure of the xenoliths reported by Mariga et al. (2006b); see their Figure 14).

The new data presented in this study, together with the studies cited above, allow us to refine the existing interpretation of the corundum-anorthite-spinel assemblage in the Rudh a' Chromain sill, and perhaps xenoliths in the LSSC more broadly. The distinction between the two textural and mineralogical portions of the xenolith made here holds for other xenoliths we have examined too. In one of these portions, the highly skeletal morphology of corundum crystals in the large plagioclase oikocrysts indicates a relatively low nucleation rate and rapid crystal growth, probably from a high viscosity Al_2O_3-oversaturated melt at relatively high temperature (>900°C). This is supported by the presence of mullite-bearing buchite pockets in the interstices between plagioclase crystals in these areas (Figure 4d; *e.g.*; Markl, 2005 and references therein). The crystallisation of corundum + plagioclase alone in the xenolith rims requires the Al_2O_3-rich melt to have a relatively simple composition. Using Theriak-Domino, it can be shown that at 1 kbar, the corundum + plagioclase assemblage is stable over a wide temperature range above ~300°C, suggesting that the key to forming the assemblage is producing the refractory rims in the first instance, rather than particularly high temperatures of metamorphism (Figure 13b). The modelling also suggests that to produce plagioclase and corundum in the proportions observed, the Al_2O_3-rich melt should have had a Al_2O_3:SiO_2 ratio of ~1:3.

The skeletal shape of the corundum is a function of low nucleation density and fast growth rates (cf. Vernon, 2004). In the other portion of the xenolith, the near perfect pseudomorphing of corundum by multiple hercynite crystals resulted from infiltration of host magma along grain boundaries and into interstitial pockets, evidenced by the greater proportion of sill groundmass material there. That the very same crystallographic relationship is hinted at between hercynite and corundum as for Ard-B-2, *i.e.*, the similar orientations between hercynite [110] and corundum facets, as well as hercynite [111] and corundum (0001), is surely more than coincidence. We suggest that hercynite nucleated epitaxially on corundum during reaction of the latter with infiltrating melt from the host sill. The grains of greater internal misorientation in the hercynite are the population of initial nucleation and rapid growth, whereas the smaller hercynite grains exhibiting a lower degree of misorientation represent subsequent growth and replacement of corundum. Similar correlations between degree of misorientation and relatively rapidly grown crystals are observed for other magmatic phases (*e.g.*, clinopyroxene; Griffiths et al., 2023) and in the material science literature (*e.g.*, Sémoroz et al., 2001). It is interesting to note that a sparse few ilmenite grains are also observed pseudomorphing parts of corundum crystals, although we did not analyse these by EBSD to compare them to their associated corundum. Plagioclase recrystallisation appears to have accompanied hercynite growth in this portion of the xenolith.

The margins of the Rudh a' Chromain xenoliths suggest they continued to be dissolved by their host magma, with ragged and irregular plagioclase boundaries and truncated corundum crystals commonly observed. That xenolith formation and late-stage dissolution occurred under relatively reducing conditions is supported by the lack of magnetite and the presence of large sulfide blebs locally attached to the edges of the xenoliths. It is also worth noting that hercynite occurs distributed throughout the sill groundmass in the vicinity of the xenolith. This suggests that assimilation of xenolith material maintained relatively reducing conditions away from the xenolith margin, and indicate contamination of the sill magma by the aluminous material. Reducing conditions may have been a function of the presence of organic material, but this would imply involvement of Mesozoic or Paleogene sedimentary rocks, rather than Neoproterozoic Moine Supergroup pelites as suggested by Preston et al. (1999), for xenoliths of the LSSC. Regardless, the presence of hercynite in the groundmass to the xenoliths represents important evidence for localised cryptic contamination of the magmas of the LSSC. However, we note that in the major element data of Preston et al. (2001), the Rudh' a' Chromain basaltic andesites do not exhibit Al_2O_3 contents markedly higher than mid-ocean ridge or other basalts, suggesting that crustal contamination may have been limited to cm-length-scales from the margins of the xenoliths.

General implications and conclusions

Although the Glebe Hill and Rudh' a' Chromain samples exhibit differences in terms of their microstructural characteristics and style of metamorphism, they also share common features that may inform more generally on the development of the corundum-anorthite-spinel assemblage. For example, corundum appears to have crystallised early in both samples, and is being replaced by ilmenite and hercynite, at Glebe Hill and Rudh' a' Chromain, respectively. Corundum morphology is different in each locality, suggesting that the nucleation and growth kinetics of each system were different, possibly a function of the degree of Al_2O_3 oversaturation in each case. Ilmenite clearly exhibits a topotactic relationship with corundum in Ard-B-2, which it replaces, reflecting relatively high Ti contents in the interstitial Fe-rich liquid in the oxide-dominated parts of this sample. However, the more subtle relationship between hercynite and corundum that is observed in the EBSD data from both Ard-B-2 and Mu-B-4 is noteworthy. It appears corundum is the earlier phase in the latter sample, but the relative timing of crystallisation of hercynite and corundum in Ard-B-2 is more difficult to constrain, despite the similarity of the crystallographic relationship between both phases in each sample. Further examination of this crystallographic relationship, between hercynite [110] and corundum facets, as well as hercynite [111] and corundum (0001), might be a productive target for future

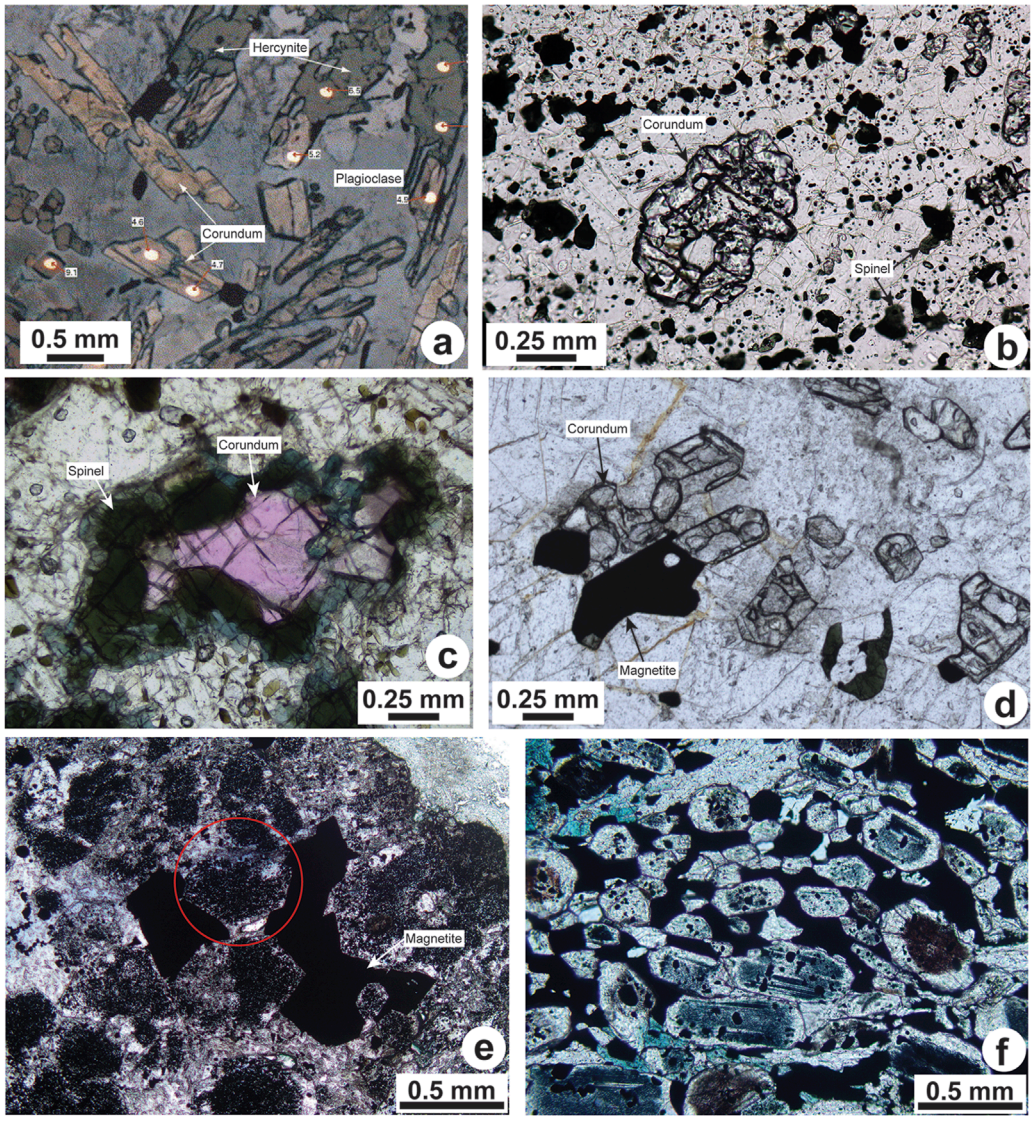

FIGURE 14
Examples of corundum-anorthite-spinel textures from different settings. **(a)** Hercynite pseudomorphs after corundum in xenoliths contained within the Voisey's Bay Intrusion, Labrador (Canada; Mariga et al., 2006a; Mariga et al., 2006b). **(b)** Corundum crystals contained within a groundmass of plagioclase and spinel in hornfels from Montecristo Island (Italy). **(c)** Corundum exhibiting reaction rims of fine-grained spinel within anorthosite layers of the Sittampundi Layered Complex (India; Karmakar et al., 2017). **(d)** Corundum within cm-sized anorthite pods hosted within amphibolites from the Granulite Terrane of Southern India, (Karmakar et al., 2020). Magnetite pseudomorphing skeletal corundum in a manner very similar to that observed in Mu-B-4. **(e,f)** Examples of emery textures from Turkey and Ontario (Canada), respectively. In **(e)**, euhedral corundum crystals (such as the one highlighted in the red circle), contain dense distributions of hercynite inclusions. Coarse-grained anhedral magnetite also occurs in interstitial pockets between the corundum grains. In **(f)**, abundant euhedral corundum crystals are characterised by blue-coloured cores and high densities of hercynite inclusions, as well as relatively colourless and inclusion free mantles. Anhedral magnetite and light blue-coloured sapphirine occur interstitially to the corundum crystals.

microstructural work aimed at understanding the crystallisation conditions of these phases.

The conditions of crystallisation of corundum, with one or more of hercynite, ilmenite and magnetite, but not necessarily with plagioclase, has been attributed to high pressure magmatic processes (Liu and Presnall, 1990), ultrahigh pressure metamorphism (Morishita and Kodera, 1998) and crustal anatexis of anorthosite (Dempster et al., 1999; Kullerud et al., 2012), but remain relatively poorly understood (Karmakar et al., 2017). An important implication of our study is that certain crystallographic relationships between corundum and spinel/oxide might be a ubiquitous phenomenon. To underscore this point, we briefly list several examples of the corundum-anorthite-spinel assemblage that bear similarities to the samples studied here, and that might profitably be investigated for their microstructural characteristics, as follows.

1. Country rock xenoliths entrained in the gabbroic-troctolitic rocks of the Voisey's Bay Intrusion, Labrador (Canada) contain examples of hercynite pseudomorphing skeletal corundum crystals, all in an interstitial plagioclase matrix, in

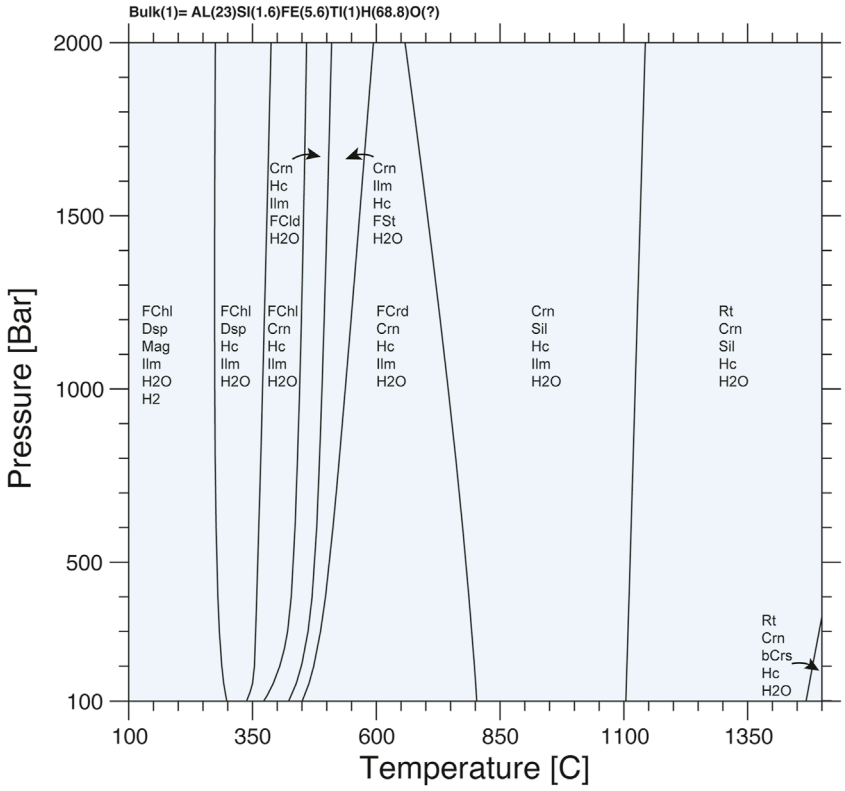

FIGURE 15
Equilibrium phase diagram for the Gove bauxite composition, calculated using Theriak-Domino with the JUN92d.bs database, for pressures of 100–2000 bars and temperatures of 100°C–1,500°C. The bulk composition used is shown at the top of the diagram. Mineral abbreviations as for previous figures and in addition: FChl, Fe-chlorite-group mineral; Dsp, diaspore; Mag, magnetite; FCld, Fe-chloritoid; FSt, Fe-staurolite; Rt, rutile; Sil, sillimanite; FCrd, Fe-cordierite; bCrs, β-cristobalite. See text for further discussion.

a similar manner to those observed in Mu-B-4 (Figure 14a; Mariga et al., 2006a; Mariga et al., 2006b). Magnetite occurs in close association with hercynite in some of the Voisey's Bay xenoliths, but does not appear to be present where hercynite pseudomorphs corundum.

2. Rocks referred to as corundum-plagioclase-spinel hornfels from Montecristo Island (Italy) exhibit a texture in which hopper and skeletal corundum crystals occur in a groundmass of hercynite and plagioclase (Figure 14b). Notably, the corundum is surrounded by plagioclase that contains relatively little spinel, and the grainsize of the spinel appears to get coarser away from the corundum crystals, suggesting a reaction relationship.
3. Various examples of Archean anorthosites contain corundum-spinel assemblages that bear remarkable similarities to those studied here. For example, corundum exhibiting reaction rims of fine-grained spinel occurs within anorthosite layers of the Sittampundi Layered Complex (India; Karmakar et al., 2017; Figure 14c). In a different example, from the Granulite Terrane of Southern India, corundum occurs within cm-sized anorthite pods hosted within anorthositic amphibolites (Karmakar et al., 2020). In this case, magnetite pseudomorphs skeletal corundum in a manner very similar to that observed in Mu-B-4 (Figure 14d), where hercynite is the secondary phase. This example indicates that the spinel phase growing at the expense of corundum need not be hercynite.
4. Schuster et al. (2023) examined the fine detail of the corundum-anorthite-spinel assemblage from the perspective of reaction rim formation, using a corundum megacryst rimmed first by spinel and then anorthite, all hosted in an alkali basalt lava flow. The formation of such spinel reaction rims has relevance to metamorphic textures and is also of specific interest to the ceramics industry; Schuster et al. (2023) showed that for their sample, the 300–400 μm thick spinel rim grew topotactially on the corundum substrate at the magmatic stage.
5. Corundum in so-called sakenites, *i.e.*, corundum-spinel-sapphirine-bearing anorthitic-to-phlogopitic rocks (Raith et al., 2008) exhibit well developed coronae of spinel and alternating zones of anorthite + corundum and anorthite + spinel, suggesting that spinel and corundum are not in equilibrium with one another.

Although there is broad consensus on the petrogenesis of the corundum-anorthite-spinel assemblage in pyrometamorphic settings, the precise detail of interpretations made by important studies such as Preston et al. (1999), Markl (2005) and Mariga et al. (2006b) differ to some extent. In particular, Markl (2005) envisaged bulk melting of Al-rich refractory residues, to form immiscible

liquid globules that subsequently quenched, whereas Preston et al. (1999) and Mariga et al. (2006b) preferred disequilibrium melting models in conjunction with granitic melt production. In anorthosite terranes, the importance of volatiles in stabilising corundum has been noted (*e.g.*, Kullerud et al., 2012; Karmakar et al., 2017); however, we do not see evidence for the involvement of a fluid phase in producing the Ard-B-2 and Mu-B-4 assemblages, so further interpretations in this regard would be speculative. As noted above for Mu-B-4, which bears textural and mineralogical similarities to the xenoliths reported by all three of the studies referred to above, for this sample we agree with an interpretation involving total fusion of refractory residues that themselves had been produced by an earlier stage of melt extraction, *i.e.*, similar to the model of Markl (2005). The Glebe Hill samples appear to have a somewhat different protolith, and resemble emery more in their overall composition (Fe- and Al-rich) than typical corundum-bearing metapelites. However, in emery, magnetite can occur with hercynite or even be the sole spinel phase (Feely et al., 2017). We have made preliminary observations on examples of emery textures that suggest hercynite and magnetite occur closely associated with corundum (Figures 14e,f) in these rocks, allowing for a crystallographic relationship such as that observed in this study; however, such a hypothesis would need to be tested on these rocks with EBSD. It does appear that corundum + hercynite are the early crystallising phases in these emery samples, with the interstitial nature of magnetite suggesting it formed later (Figures 14e,f). We took a bauxite bulk composition (from the Gove deposit, Australia; Patterson et al., 1986) and using Theriak-Domino, produced a pseudosection to evaluate a range of equilibrium assemblages between 100°C–1,500°C and 0.1–2 kbar (Figure 15). The results indicate that hercynite forms in conjunction with corundum at relatively low temperature (*i.e.*, ~350°C) and remains stable up to 1,500°C for most of the range of pressure modelled. Hercynite is sufficient to take up most of the FeO in the bulk bauxite for a large part of the range of pressure and temperature shown, which given that Gove is a relatively high Fe-content bauxite (~17 wt%; Patterson et al., 1986) has interesting implications for what the drivers for magnetite crystallisation might be. We suggest that future work might usefully be directed toward developing our understanding of the coexistence of corundum + hercynite + magnetite in emery, to investigate the possibility that interstitial magnetite forms after crystallisation of the other two phases in response to local (microstructural)-scale excesses in Fe_3O_4 content in the rocks.

Data availability statement

The original contributions presented in the study are included in the article/Supplementary Material, further inquiries can be directed to the corresponding author.

Author contributions

BO'D: Conceptualization, Data curation, Formal Analysis, Funding acquisition, Investigation, Methodology, Project administration, Resources, Validation, Visualization, Writing – original draft, Writing – review and editing. HH: Formal Analysis, Funding acquisition, Investigation, Methodology, Resources, Software, Writing – original draft, Writing – review and editing.

Funding

The author(s) declare that financial support was received for the research and/or publication of this article. BO'D acknowledges current research support from the Natural Sciences and Engineering Research Council of Canada (NSERC Discovery Grant) and from the Newmont Chair in Economic Geology (University of Ottawa). HH acknowledges research funding from the Centre National de la Recherche Scientifique (CNRS).

Acknowledgments

James Westland is thanked for the field photographs shown in Figures 2b,c. Alessandro Da Mommio is thanked for his permission to use the photomicrograph shown in Figure 11b. Shreya Karmakar is similarly thanked for the photomicrographs shown in Figures 11c,d. The reuse of the image from Mariga et al. (2006a) was permitted by Elsevier (via license number 5906570824290 to BO'D). We thank Arnaud Proietti, Philippe de Parseval and Françoise Maubé for assistance during data collection. Georges Ceuleneer is thanked for insightful and constructive comments on an early version of the manuscript. The constructive and detailed comments of Chiara Groppo Torino and Javier Garcia Serrano helped improve the original version of the manuscript, as did the editorial guidance of Simona Ferrando.

Conflict of interest

The authors declare that the research was conducted in the absence of any commercial or financial relationships that could be construed as a potential conflict of interest.

Generative AI statement

The author(s) declare that no Generative AI was used in the creation of this manuscript.

Publisher's note

Supplementary material

The Supplementary Material for this article can be found online at: https://www.frontiersin.org/articles/10.3389/feart.2025.1576938/full#supplementary-material

References

Bachmann, F., Hielscher, R., and Schaeben, H. (2010). Texture analysis with MTEX – free and open source software toolbox. *Solid State Phenom.* 160, 63–68. doi:10.4028/www.scientific.net/SSP.160.63

Bachmann, F., Hielscher, R., and Schaeben, H. (2011). Grain detection from 2d and 3d EBSD data—specification of the MTEX algorithm. *Ultramicroscopy* 111, 1720–1733. doi:10.1016/j.ultramic.2011.08.002

Bailey, E. B., Clough, C. T., Wright, W. B., Richey, J. E., and Wilson, G. V. (1924). *Tertiary and post-tertiary geology of mull, loch aline, and oban*. Edinburgh, Scotland: Memoir Geological Survey.

Bell, B. R., and Williamson, I. T. (2002). Tertiary igneous activity. In: N. H. Trewin, editor. *The geology of Scotland*. 4th edition. London, UK: Geological Society of London. p. 371–408.

Buist, D. S. (1959). The composite sill of Rudh' an eireannaich, skye. *Geol. Mag.* 96, 247–252. doi:10.1017/s0016756800060234

Buist, D. S. (1961). The composite sill of Rudh' a' Chromain, Carsaig, Mull. *Geol. Mag.* 98, 67–76. doi:10.1017/s001675680000008x

Day, S. J. (1989). *The geology of the hyperstheme Gabbro of Ardnamurchan point and implications for its evolution as an upper crustal basic magma chamber*. Durham, UK: Durham University.

De Capitani, C., and Brown, T. H. (1987). The computation of chemical equilibrium in complex systems containing non-ideal solutions. *Geochimica. Cosmochimica. Acta* 51, 2639–2652. doi:10.1016/0016-7037(87)90145-1

De Capitani, C., and Petrakakis, K. (2010). The computation of equilibrium assemblage diagrams with Theriak/Domino software. *Am. Mineralogist* 95, 1006–1016. doi:10.2138/am.2010.3354

Dempster, T. J., Preston, R. J., and Bell, B. R. (1999). The origin of Proterozoic massif-type anorthosites: evidence from interactions between crustal xenoliths and basaltic magma. *J. Geol. Soc.* 156, 41–46. doi:10.1144/gsjgs.156.1.0041

Droop, G. T. R. (1987). A general equation for estimating Fe3+ concentrations in ferromagnesian silicates and oxides from microprobe analyses using stoichiometric criteria. *Mineral. Mag.* 51, 431–435. doi:10.1180/minmag.1987.051.361.10

Duchesne, J. C. (1996). Liquid ilmenite or liquidus ilmenite: a comment on the nature of ilmenite vein deposits. In: M. Jean, and D. Demaiffe, editor. *Petrology and geochemistry of magmatic suites of rocks in the continental and oceanic crusts*. Brussels: MRAC-ULB. p. 73–82.

Emeleus, C. H., and Bell, B. R. (2005). *British regional geology: the Palaeogene volcanic districts of Scotland*. 4th edition. Nottingham: British Geological Survey.

Feely, M., Leake, B. E., Costanzo, A., Cassidy, P., and Walsh, B. (2017). Sapphire occurrences in Connemara: field and mineralogical descriptions from an erratic, and from bedrock pelitic xenoliths in the Grampian metagabbro-gneiss suite. *Ir. J. Earth Sci.* 35, 45–54. doi:10.3318/ijes.2017.35.45

Frost, B. R. (1991). Introduction to oxygen fugacity and its petrologic importance. In: D. H. Lindsley, editor. *Oxide minerals: petrologic and magnetic significance. Reviews in mineralogy*. Chantilly, Virginia: Mineralogical Society of America, Vol. 25. p. 1–10.

Geikie, A. (1861). *On the chronology of the trap-rocks of Scotland*. Edinburgh, Scotland: Transactions of the Royal Society of Edinburgh. p. 63.

Geikie, A. (1897). *The ancient volcanoes of Great Britain*. London, UK: Macmillan.

Grapes, R. (2011). *Pyrometamorphism*. 2nd edition. Berlin: Springer-Verlag. p. 365.

Gribble, C. D. (1976). *Ardnamurchan; a guide to geological excursions*. Edinburgh, Scotland: Edinburgh Geological Society. p. 122.

Griffiths, T. A., Habler, G., Ageeva, O., Sutter, C., Ferrière, L., and Abart, R. (2023). The origin of lattice rotation during dendritic crystallization of clinopyroxene. *J. Petrol.* 64 (1), 1–19. doi:10.1093/petrology/egac125

Harker, A. (1904). *The tertiary igneous rocks of skye*. Edinburgh, Scotland: Memoirs of the Geological Survey.

Henry, H. (2018). *Mantle pyroxenites: deformation and seismic properties*. New South Wales, Australia: Macquarie University and Université Toulouse.

Holness, M. B., Vukmanovic, Z., and Mariani, E. (2017). Assessing the role of compaction in the formation of adcumulates: a microstructural perspective. *J. Petrology* 58, 643–673. doi:10.1093/petrology/egx037

Karmakar, S., Mukerjee, S., Sanyal, S., and Sengupta, P. (2017). Origin of peraluminous minerals (corundum, spinel, and sapphirine) in a highly calcic anorthosite from the Sittampundi Layered Complex, Tamil Nadu, India. *Contributions Mineralogy Petrology* 172, 67. doi:10.1007/s00410-017-1383-8

Karmakar, S., Mukherjee, S., and Dutta, U. (2020). Origin of corundum within anorthite megacrysts from anorthositic amphibolites, Granulite Terrane, Southern India. *Am. Mineralogist* 105, 1161–1174. doi:10.2138/am-2020-7108

Kullerud, K., Nasipuri, P., Ravna, E. J. K., and Selbekk, R. S. (2012). Formation of corundum megacrysts during H2O-saturated incongruent melting of feldspar: P–T pseudosection-based modelling from the Skattøra migmatite complex, North Norwegian Caledonides. *Contributions Mineralogy Petrology* 164, 627–641. doi:10.1007/s00410-012-0765-1

Lino, L. M., Carvalho, P. R., Vlach, S. R. F., and Quiroz-Valle, F. R. (2023). Evidence for silicate liquid immiscibility in recharging, alkali-rich tholeiitic systems: the role of unmixing in the petrogenesis of intermediate, layered plutonic bodies and bimodal volcanic suites. *Lithos* 450-451, 107193. doi:10.1016/j.lithos.2023.107193

Liu, T. C., and Presnall, D. C. (1990). Liquidus phase relationships on the join anorthite-forsterite-quartz at 20 kbar with applications to basalt petrogenesis and igneous sapphirine. *Contributions Mineralogy Petrology* 104, 735–742. doi:10.1007/bf01167290

Mariga, J., Ripley, E. M., and Li, C. (2006b). Petrologic evolution of gneissic xenoliths in the Voisey's Bay Intrusion, Labrador, Canada: mineralogy, reactions, partial melting, and mechanisms of mass transfer. *Geochem. Geophys. Geosystems* 7 (5), Q05013. doi:10.1029/2005gc001184

Mariga, J., Ripley, E. M., Li, C., McKeegan, K. D., Schmidt, A., and Groove, M. (2006a). Oxygen isotopic disequilibrium in plagioclase–corundum–hercynite xenoliths from the Voisey's Bay Intrusion, Labrador, Canada. *Earth Planet. Sci. Lett.* 248, 263–275. doi:10.1016/j.epsl.2006.05.031

Markl, G. (2005). Mullite-corundum-spinel-cordierite-plagioclase xenoliths in the Skaergaard Marginal Border Group: multi-stage interaction between metasediments and basaltic magma. *Contributions Mineralogy Petrol.* 149, 196–215. doi:10.1007/s00410-004-0644-5

Morishita, T., and Kodera, T. (1998). Finding of corundum-bearing gabbro boulder possibly derived from the Horoman Peridotite Complex, Hokkaido, northern Japan. *J. Mineralogy, Petrology Econ. Geol.* 93, 52–63. doi:10.2465/ganko.93.52

Naslund, H. R. (1983). The effect of oxygen fugacity on liquid immiscibility in iron-bearing silicate melts. *Am. J. Sci.* 283, 1034–1059. doi:10.2475/ajs.283.10.1034

O'Driscoll, B. (2007). The Centre 3 layered gabbro intrusion, Ardnamurchan, NW Scotland. *Geol. Mag.* 144 (6), 897–908. doi:10.1017/s0016756807003846

Patterson, S. H., Kurtz, H. F., Olson, J. C., and Neeley, C. L. (1986). *World bauxite resources: geology and resources of aluminum*. Reston, VA: U.S. Geological Survey Professional Paper 1076-B, 130.

Preston, R. J. (2001). Composite minor intrusions as windows into subvolcanic magma reservoir processes: mineralogical and geochemical evidence for complex magmatic plumbing systems in the British Tertiary Igneous Province. *J. Geol. Soc.* 158, 47–58. doi:10.1144/jgs.158.1.47

Preston, R. J., and Bell, B. R. (1997). Cognate gabbroic xenoliths from a tholeiitic subvolcanic sill complex: implications for fractional crystallization and crustal contamination processes. *Mineral. Mag.* 61, 329–349. doi:10.1180/minmag.1997.061.406.01

Preston, R. J., Bell, B. R., and Rogers, G. (1998). The Loch Scridain Xenolithic Sill Complex, Isle of Mull, Scotland: fractional crystallization, assimilation, magma-mixing and crustal anatexis in subvolcanic conduits. *J. Petrology* 39, 519–550. doi:10.1093/petrology/39.3.519

Preston, R. J., Dempster, T. J., Bell, B. R., and Rogers, G. (1999). The petrology of mullite-bearing peraluminous xenoliths; implications for contamination processes in basaltic magmas. *J. Petrol.* 40, 549–573. doi:10.1093/petroj/40.4.549

Prior, D. J., Boyle, A. P., Brenker, F., Cheadle, M. C., Day, A., Lopez, G., et al. (1999). The application of electron backscatter diffraction and orientation contrast imaging in the SEM to textural problems in rocks. *Am. Mineralogist* 84 (11-12), 1741–1759. doi:10.2138/am-1999-11-1204

Raith, M. M., Rakotondrazafy, R., and Sengupta, P. (2008). Petrology of corundum-spinel-sapphirine-anorthite rocks (sakenites) from the type locality in southern Madagascar. *J. Metamorph. Geol.* 26, 647–667. doi:10.1111/j.1525-1314.2008.00779.x

Richey, J. E., and Thomas, H. H. (1930). *The geology of ardnamurchan, north-west mull and coll. Memoir of the geological survey of great britain(Scotland)*. Scotland. Edinburgh: HMSO for the Geological Survey. p. 393.

Satsukawa, T., Ildefonse, B., Mainprice, D., Morales, L. F. G., Michibayashi, K., and Barou, F. (2013). A database of plagioclase crystal preferred orientations (CPO) and microstructures – implications for CPO origin, strength, symmetry and seismic anisotropy in gabbroic rocks. *Solid. Earth.* 4, 511–542. doi:10.5194/se-4-511-2013

Schuster, R., Tiede, L., Ageeva, O., Griffiths, T. A., Abart, R., and Habler, G. (2023). Microstructure and texture of a spinel corona around a basalt hosted corundum xenocrystal. *J. Petrol.* 64, 1–18. doi:10.1093/petrology/egac130

Sémoroz, A., Durandet, Y., and Rappaz, M. (2001). EBSD characterization of dendrite growth directions, texture and misorientations in hot-dipped Al-Zn-–Si coatings. *Acta Mater.* 49, 529–541. doi:10.1016/s1359-6454(00)00322-0

Smith, J. V. (2013). *Feldspar minerals: crystal structure and physical properties 1*. Berlin, Heidelberg: Springer Science and Business Media.

Thomas, H. H. (1922). On certain xenolithic Tertiary minor intrusions in the Island of Mull (Argyllshire). *Quat. J. Geol. Soc. Lond.* 78, 229–260. doi:10.1144/gsl.jgs.1922.078.01-04.07

Turnock, A. C., and Eugster, H. P. (1962). Fe-Al oxides: phase relationships below 1,000 °C. *J. Petrol.* 3 (3), 533–565. doi:10.1093/petrology/3.3.533

Van Hinsberg, V., Yakymchuk, C., Kleist Jepsen, A. T., Kirkland, C. L., and Szilas, K. (2021). The corundum conundrum: constraining the compositions of fluids involved in ruby formation in metamorphic melanges of ultramafic and aluminous rocks. *Chem. Geol.* 571, 120180. doi:10.1016/j.chemgeo.2021.120180

Vernon, R. H. (2004). *A practical guide to rock microstructure*. Cambridge: Cambridge University Press. p. 594.

Voudouris, P., Mavrogonatos, C., Graham, I., Giuliani, G., Melfos, V., Karampelas, S., et al. (2019). Gem corundum deposits of Greece: geology, mineralogy and genesis. *Minerals* 9 (49), 49. doi:10.3390/min9010049

Wells, M. K. (1951). Sedimentary inclusions in the hypersthene-gabbro, ardnamurchan, argyllshire. *Mineral. Mag.* 29 (214), 715–736. doi:10.1180/minmag.1951.029.214.04

Winchell, A. N. (1951). *Elements of optical mineralogy: an introduction to microscopic petrology*. London, UK: Chapman and Hall Ltd. p. 1–551.

Zhao, D., Essene, E. J., and Zhang, Y. (1999). An oxygen barometer for rutile-ilmenite assemblages: oxidation state of metasomatic agents in the mantle. *Earth Planet. Sci. Lett.* 166, 127–137. doi:10.1016/s0012-821x(98)00281-7